

Ridging, Strength, and Stability in High-Resolution Sea Ice Models

William H. Lipscomb and Elizabeth C. Hunke

Group T-3, Los Alamos National Laboratory, Los Alamos, New Mexico, USA

Wieslaw Maslowski and Jaromir Jakacki

Department of Oceanography, Naval Postgraduate School, Monterey, California, USA

Submitted to *Journal of Geophysical Research*

June 16, 2006

Abstract

In multi-category sea ice models the compressive strength of the ice pack is often assumed to be proportional to the potential energy of pressure ridges. This assumption, combined with other standard features of ridging schemes, allows the ice strength to change dramatically on short time scales. In high-resolution (~ 10 km) sea ice models with a typical time step (~ 1 hour), abrupt strength changes can lead to large internal stress gradients that destabilize the flow. The unstable flow is characterized by large oscillations in ice concentration, thickness, strength, velocity, and strain rates. Straightforward, physically motivated changes in the ridging scheme can reduce the likelihood of abrupt strength changes and improve stability. In simple test problems with flow toward and around topography, stability is significantly enhanced by eliminating the threshold fraction G^* in the ridging participation function. Use of an exponential participation function increases the maximum stable time step at 10-km resolution from less than 30 minutes to about 2 hours. Modifying the redistribution function to build thinner ridges gives modest gains in stability and also improves agreement between modeled and observed thickness distributions. Allowing the ice strength to vary linearly with the mean ice thickness enhances stability but probably underestimates the maximum stresses.

1. Introduction

Sea ice models typically consist of a thermodynamic component, which computes vertical heat conduction, growth, and melting, and a dynamic component, which determines horizontal motion. Both thermodynamic and dynamic properties depend on the ice thickness, which can vary from less than a centimeter to several meters. In order to better represent thickness-dependent processes, many sea ice models in recent years have introduced an ice thickness distribution (ITD). The evolution of the ITD can be described following *Thorndike et al.* [1975] as

$$\frac{\partial g}{\partial t} = -\nabla \bullet (\mathbf{u}g) - \frac{\partial}{\partial h}(fg) + \psi, \quad (1)$$

where h is the ice thickness, $g(h, \mathbf{x}, t)$ is a probability distribution function for thickness, $\mathbf{u} = (u, v)$ is the horizontal velocity, $f = dh/dt$ is the thermodynamic growth rate, and ψ is a function to be specified. The first term on the RHS describes horizontal transport; the second term describes thermodynamic transport in thickness space h ; and the last term describes mechanical redistribution in thickness space.

The velocity \mathbf{u} is computed from a momentum equation that includes the effects of winds, ocean currents, sea surface tilt, the Coriolis force, and internal ice stress. Much research has focused on parameterizing the internal stress term in a realistic way. Following *Hibler* [1979; henceforth *H79*], many sea ice models treat the ice pack as a viscous-plastic material that has strength under convergence and shearing, but offers little or no resistance to divergence. Various solution methods have been developed. One class of methods [e.g., *Zhang and Hibler*, 1997; *Zhang and Rothrock*, 2000] solves the momentum equation implicitly over the entire ice pack. Another method, the elastic-viscous-plastic (EVP) scheme of *Hunke and Dukowicz* [1997], introduces an elastic term as a numerical artifice so that the solution can be computed explicitly. Both approaches have been shown to give stable, accurate solutions.

Much less effort has focused on ψ , which determines how ice is redistributed among thickness categories by mechanical processes such as rafting and pressure ridging. (In this paper we will generally refer to all such mechanical processes as “ridging.”) Current ridging schemes are

largely heuristic and are difficult to verify empirically. Our starting point for this paper is the ridging scheme used in CICE, the Los Alamos sea ice model [Hunke and Lipscomb, 2004]. This scheme is based on the work of Rothrock [1975; henceforth *R75*], Thorndike *et al.* [1975; henceforth *T75*], Hibler [1980], and Flato and Hibler [1995], who used a combination of observations, mathematical reasoning, and physical intuition to develop ridging parameterizations suitable for multi-category sea ice models. We refer to this scheme as the standard ridging scheme.

In some models, including CICE, the ridging scheme is closely connected to the dynamics through the ice strength. Following *R75*, these models assume that the ice strength (defined as the compressive stress below which the ice is rigid and at which it fails) is a function of the energy dissipated during ridge creation. The energy dissipation rate depends in turn on the participation of various thickness categories in ridging and on the thickness of the resulting ridges. For example, a model that generates thick ridges will have stronger ice and larger stresses than a model that builds thinner ridges. Larger stresses result in smaller velocities and strain rates. To date there has been little study of the relation between ridging and dynamics in sea ice models.

Global climate models typically have a horizontal resolution of 1° or more for sea ice and the underlying ocean. There is increasing interest, however, in running sea ice and ocean models at scales of the order of 10 km (about 0.1°) or less. These small scales are necessary to resolve mesoscale eddies in the ocean [Smith *et al.*, 2000] and detailed features of sea ice motion [e.g., Maslowski and Lipscomb, 2003]. In ocean and atmosphere models, the time step Δt and grid cell size Δx must satisfy a Courant-Friedrichs-Lewy (CFL) condition of the form $\Delta x \leq \max(|\mathbf{u}|)\Delta t$, where $|\mathbf{u}|$ is the greatest physical speed allowed by the model equations (for example, the speed of gravity waves). When the time step exceeds the CFL limit at a given spatial resolution, the model becomes inaccurate and often unstable. We show in this paper that sea ice models have an analogous limit, which depends on the time and spatial scales at which the ice strength changes. This limit is especially acute for high-resolution models that use the *R75* ice strength formulation.

Section 2 summarizes the dynamics and ridging schemes used in CICE, and section 3 describes model behavior when the stability limit is violated. We explain the source of the insta-

bility in section 4, using a one-dimensional test case to simplify the analysis. In section 5 we show that model stability can be improved by changing the ridging participation function and the thickness distribution of ridges. Although our motivation is primarily numerical, these changes can also be justified on physical grounds. Section 6 concludes the analysis and discusses some remaining uncertainties.

2. Dynamics and ridging in CICE

The results in this paper were obtained using CICE version 3.1 [Hunke and Lipscomb, 2004], modified as needed to study model stability. CICE has been used for many regional and global climate studies, and its components have been adopted by the Community Climate System Model [Holland *et al.*, 2006] and by HadGEM1, the latest version of the UK Hadley Centre climate model [McLaren *et al.*, 2006]. CICE is normally run with five ice thickness categories plus open water to approximate the continuous ITD described by (1). The model includes EVP dynamics [Hunke and Dukowicz, 1997, 2002], an incremental remapping advection scheme [Lipscomb and Hunke, 2004], multilayer energy-conserving thermodynamics [Bitz and Lipscomb, 1999], a remapping scheme for ice thickness [Lipscomb, 2001], and the standard ridging scheme of $T75$, $R75$, and others. Here we summarize the key features of the dynamics and ridging schemes.

2.1. Ice dynamics

The EVP dynamics scheme solves the 2D sea ice momentum equation, which can be written schematically in Cartesian coordinates as

$$m \frac{\partial u}{\partial t} = F_x + \tau_x, \quad (2)$$

$$m \frac{\partial v}{\partial t} = F_y + \tau_y, \quad (3)$$

where m is the ice mass per unit area, F_x and F_y are internal ice forces, and τ_x and τ_y denote external forcing due to wind stress, ocean stress, sea surface tilt, and the Coriolis effect. The internal forces are given by the stress divergence:

$$F_x = \frac{\partial \sigma_{11}}{\partial x} + \frac{\partial \sigma_{12}}{\partial y}, \quad (4)$$

$$F_y = \frac{\partial \sigma_{12}}{\partial x} + \frac{\partial \sigma_{22}}{\partial y}, \quad (5)$$

where σ_{11} , σ_{12} , and σ_{22} are the components of the symmetric 2D stress tensor.

The stresses are assumed to be functions of regional-scale strain rates. This hypothesis is consistent with measurements of stress and deformation in the Arctic ice pack [Richter-Menge *et al.*, 2002]. In the standard viscous-plastic (VP) model of *H79*, the stresses are related to the strain rates by

$$\hat{\sigma}_1 = 2\zeta D_D - P, \quad \hat{\sigma}_2 = 2\eta D_T, \quad \hat{\sigma}_{12} = \eta D_S, \quad (6)$$

where P is the compressive ice strength, $\hat{\sigma}_1 = \sigma_{11} + \sigma_{22}$, $\hat{\sigma}_2 = \sigma_{11} - \sigma_{22}$, $\hat{\sigma}_{12} = \sigma_{12}$, ζ is the bulk viscosity, and η is the shear viscosity. (We follow the notation of *Hunke and Dukowicz* [2002], except that carets are added to avoid confusion with the principal stresses σ_1 and σ_2 .)

The strain rates on the RHS are defined as

$$D_D = \dot{\epsilon}_{11} + \dot{\epsilon}_{22} = \frac{\partial u}{\partial x} + \frac{\partial v}{\partial y}, \quad (7)$$

$$D_T = \dot{\epsilon}_{11} - \dot{\epsilon}_{22} = \frac{\partial u}{\partial x} - \frac{\partial v}{\partial y}, \quad (8)$$

$$D_S = 2\dot{\epsilon}_{12} = \frac{\partial u}{\partial y} + \frac{\partial v}{\partial x}, \quad (9)$$

where $\dot{\epsilon}_{11}$, $\dot{\epsilon}_{12}$, and $\dot{\epsilon}_{22}$ are the components of the 2D strain rate tensor. The viscosities are given by

$$\zeta = \frac{P}{2\Delta}, \quad \eta = \frac{P}{2e^2\Delta}, \quad (10)$$

where Δ is defined as

$$\Delta = [D_D^2 + (D_T^2 + D_S^2)/e^2]^{1/2}, \quad (11)$$

and e is the ratio between the maximum compressive strength and the maximum shear strength. CICE follows *H79* in setting $e = 2$. For very small strain rates the model is regularized by replacing Δ in (10) with a minimum value Δ_{\min} , which prevents the viscosities from growing without bound. The rate of energy dissipation by internal ice forces is given by contracting the stress and strain rate tensors:

$$\sigma_{ij} \dot{\epsilon}_{ij} = \frac{1}{2}(\hat{\sigma}_1 D_D + \hat{\sigma}_2 D_T) + \hat{\sigma}_{12} D_S = \frac{P}{2}(\Delta - D_D), \quad (12)$$

which follows from (6)–(11).

The EVP model introduces a time-dependent elastic term that improves accuracy on short time scales and allows the equations to be solved explicitly. With this term, the stress equations (6) are replaced by

$$\frac{1}{E} \frac{\partial \hat{\sigma}_1}{\partial t} + \frac{\hat{\sigma}_1}{2\zeta} + \frac{P}{2\zeta} = D_D, \quad (13)$$

$$\frac{1}{E} \frac{\partial \hat{\sigma}_2}{\partial t} + \frac{\hat{\sigma}_2}{2\eta} = D_T, \quad (14)$$

$$\frac{1}{E} \frac{\partial \hat{\sigma}_{12}}{\partial t} + \frac{\hat{\sigma}_{12}}{2\eta} = \frac{1}{2} D_S, \quad (15)$$

where E is an elastic parameter that can vary in time and space. These equations reduce to the VP equations at steady state. The equations are discretized on the B-grid, with strain rates, strength, and stress defined at cell centers and velocity at cell corners. At the beginning of each time step, the strength P is computed based on the ridging parameterization. The momentum and stress equations are subcycled, typically 120 times per time step, with the stresses, viscosities, and velocities updated during each subcycle but with P held fixed. Elastic waves are damped during the subcycling so that the solution reaches steady state except in compact regions with small deformation rates. More details may be found in *Hunke and Dukowicz [1997, 2002]* and *Hunke [2001]*.

2.2. Ridging

The ridging scheme gives the form of the redistribution function ψ in (1). The standard ridging scheme used in CICE has four components: (1) a rule for computing the rates of opening, closing, and ridging, given the strain rates; (2) a function $a(h)$ that describes the thickness distribution of ice participating in ridging, given $g(h)$; (3) a function $n(h)$ that describes the thickness distribution of the resulting ridged ice, given $a(h)$; and (4) a procedure for computing the ice strength P , given $a(h)$ and $n(h)$. We describe these components in turn.

First, it is useful to define two strain rate invariants, the divergence $\dot{\epsilon}_I$ and shear $\dot{\epsilon}_{II}$, which depend on the spatial derivatives of u and v :

$$\dot{\epsilon}_I = \frac{\partial u}{\partial x} + \frac{\partial v}{\partial y}, \quad \dot{\epsilon}_{II} = \sqrt{\left(\frac{\partial u}{\partial x} - \frac{\partial v}{\partial y}\right)^2 + \left(\frac{\partial u}{\partial y} + \frac{\partial v}{\partial x}\right)^2}. \quad (16)$$

Referring to (7)–(9) and (11), note that $\dot{\epsilon}_I \equiv D_D$, $\dot{\epsilon}_{II} \equiv \sqrt{D_T^2 + D_S^2}$, and $\Delta \equiv \sqrt{\dot{\epsilon}_I^2 + \dot{\epsilon}_{II}^2}/e^2$. The divergence and shear can be combined to form another pair of invariants:

$$|\dot{\epsilon}| = \sqrt{\dot{\epsilon}_I^2 + \dot{\epsilon}_{II}^2}, \quad \theta = \text{atan}(\dot{\epsilon}_{II}/\dot{\epsilon}_I), \quad (17)$$

where $|\dot{\epsilon}|$ is the strain rate magnitude and θ gives the relative contributions of divergence and shear. We have $\theta = 0, \pi/2$, and π for pure divergence, shear, and convergence, respectively.

Next we specify the form of ψ . When the pack is diverging and ice is leaving a given region, ψ replaces ice with open water. When the pack is converging, ψ reduces the open water area and deforms thin ice into thick ridges. Under shear, ψ may generate a combination of opening, closing, and ridging. T75 proposed that for any strain rate, ψ must satisfy two constraints:

$$\int_0^\infty \psi \, dh = \dot{\epsilon}_I, \quad \int_0^\infty h \, \psi \, dh = 0, \quad (18)$$

which enforce conservation of area and volume, respectively. Under pure divergence, ψ is given by a delta function at $h = 0$, corresponding to creation of open water:

$$\psi = \delta(h) \dot{\epsilon}_I. \quad (19)$$

For pure convergence, ψ can be written as

$$\psi = w_r(h, g) |\dot{\epsilon}_I|, \quad (20)$$

where w_r is known as the ridging mode. From (18), w_r must satisfy

$$\int_0^\infty w_r dh = -1, \quad \int_0^\infty h w_r dh = 0. \quad (21)$$

For the general case including shear, T75 proposed

$$\psi = |\dot{\epsilon}| [\alpha_o(\theta) \delta(h) + \alpha_r(\theta) w_r], \quad (22)$$

where α_o and α_r are coefficients for opening and ridging/closing, respectively. Equation (22) reduces to (19) for pure divergence provided that $\alpha_o(0) = 1$ and $\alpha_r(0) = 0$. Similarly, (22) reduces to (20) for pure convergence if $\alpha_o(\pi) = 0$ and $\alpha_r(\pi) = 1$.

It remains to determine α_r and α_o for general θ . R75 showed that α_r can be derived from the yield curve (the curve in 2D stress space that describes when plastic failure occurs). For the standard VP ice rheology, the stresses lie on an elliptical yield curve [Hibler, 1977]:

$$\left[\frac{\sigma_1 + \sigma_2 + P}{P} \right]^2 + \left[\frac{\sigma_2 - \sigma_1}{(P/e)} \right]^2 = 1, \quad (23)$$

where σ_1 and σ_2 are the principal components of the 2D stress tensor. For this yield curve, α_r is given by [Stern *et al.*, 1995]

$$\alpha_r(\theta) = -\frac{1}{2} \cos \theta + \frac{1}{2} \sqrt{\cos^2 \theta + (\sin^2 \theta)/e^2}. \quad (24)$$

From (17), $\cos \theta = \dot{\epsilon}_I/|\dot{\epsilon}|$ and $\sin \theta = \dot{\epsilon}_{II}/|\dot{\epsilon}|$. Thus (24) can be rewritten as

$$\alpha_r = \frac{1}{2|\dot{\epsilon}|} [\Delta - \dot{\epsilon}_I], \quad (25)$$

where Δ is given by (11). Inserting (22) into the first equation of (18) and using the first equation of (21), we obtain an expression for α_o :

$$\alpha_o = \alpha_r + \cos \theta. \quad (26)$$

From (25) the rate of ridging/closing is

$$|\dot{\epsilon}| \alpha_r = \frac{1}{2} (\Delta - \dot{\epsilon}_I). \quad (27)$$

Comparing (27) to (12), we see that the rate of energy dissipation by internal ice forces is equal to the product of the ridging/closing rate and the ice strength. Equation (27) can be rewritten as

$$|\dot{\epsilon}| \alpha_r = \frac{1}{2}(\Delta - |\dot{\epsilon}_I|) - \min(\dot{\epsilon}_I, 0), \quad (28)$$

in which the first term on the RHS accounts for shear and the second term accounts for convergence. *Flato and Hibler* [1995] suggested that the first term should be multiplied by a factor $C_s < 1$ to allow for energy sinks other than ridge-building (e.g., sliding friction) during shear. They estimated $C_s = 0.5$, but this value is not well constrained by observations.

Following *T75*, the ridging mode can be written as

$$w_r = \frac{-a(h) + n(h)}{N}, \quad (29)$$

where $a(h)$ is the ITD of ice participating in ridging, $n(h)$ is the ITD of the resulting ridged ice, and N is a normalization factor required to conserve area. Ice of thickness h can ridge only if $g(h) > 0$; this is guaranteed by writing $a(h) = b(h)g(h)$, where $b(h)$ is a weighting function. Intuitively, $b(h)$ should be weighted toward the thin end of the ITD, so that leads will close and thin ice will ridge before thicker ice can ridge. *T75* proposed

$$b(h) = \begin{cases} \frac{2}{G^*} \left[1 - \frac{G(h)}{G^*} \right], & 0 \leq G(h) \leq G^* \\ 0, & G(h) > G^* \end{cases} \quad (30)$$

where the cumulative thickness distribution function G is defined as

$$G(h) = \int_0^h g(h) dh. \quad (31)$$

The parameter G^* is the maximum value of $G(h)$ for which ice participates in ridging. Thus the probability that ice of thickness h will participate in ridging decreases linearly with G from a maximum at $G = 0$ to zero at $G = G^*$. When the open water fraction exceeds G^* , there is no ridging of ice, but only closing of leads (i.e., ice with $h = 0$). Most models, including CICE, have set $G^* = 0.15$ as in *T75*.

Again following *T75*, the ITD of newly ridged ice can be written as

$$n(h) = \int_0^\infty a(h_1) \gamma(h_1, h) dh_1, \quad (32)$$

where $\gamma(h_1, h) dh$ is the ice area ridged to the thickness interval $(h, h + dh)$ per unit area lost by ice of thickness h_1 . Volume conservation implies

$$\int_0^\infty h \gamma(h_1, h) dh = h_1. \quad (33)$$

Noting that ridge keels are roughly triangular, *Hibler* [1980] proposed

$$\gamma(h_1, h) = \begin{cases} \frac{1}{2(H^* - h_1)}, & 2h_1 \leq h \leq 2\sqrt{H^* h_1} \\ 0, & h < 2h_1 \text{ or } h > 2\sqrt{H^* h_1} \end{cases} \quad (34)$$

where H^* is an empirical thickness. That is, γ is uniform in a range between $h_{\min} = 2h_1$, corresponding to rafting, and $h_{\max} = 2\sqrt{H^* h_1}$. The square root dependence of h_{\max} on h_1 is based on the assumption that all ridges have similar slope angles independent of thickness. *Hibler* [1980] suggested $H^* = 100$ m based on mechanistic modeling by *Parmeter and Coon* [1972]. *Flato and Hibler* [1995] also recommended $H^* = 100$ m, citing measurements of block sizes in first-year ridges by *Tucker et al.* [1984]. CICE 3.1 is often run with $H^* = 25$ m, which gives thinner ridges in better agreement with observations of ridged multiyear ice. (Like most models, CICE has no mechanism for transforming porous first-year ridges into consolidated older ridges.) In the experiments below, we follow *Flato and Hibler* [1995] and take $H^* = 100$ m as the standard value. CICE differs from (34) in one respect: The minimum ridge thickness is limited by $h_{\min} = \min(2h_1, h_1 + h_{\text{raft}})$, where $h_{\text{raft}} = 1$ m is the thickest ice allowed to raft. Thicker ice is assumed to ridge by other means, such as crushing. Since most ridging ice has a thickness of ~ 1 m or less, model results are not very sensitive to this change.

This completes the description of the standard ridging scheme in terms of the continuous function $g(h)$. In CICE, $g(h)$ is discretized by specifying the fractional area A_n and thickness h_n in each of N_c categories (usually $N_c = 5$), along with the open water fraction A_0 . The fixed lower and upper boundaries of category n are H_{n-1} and H_n , respectively. In this paper we set

$H_n = (0.0 \text{ m}, 0.6 \text{ m}, 1.4 \text{ m}, 2.4 \text{ m}, 3.6 \text{ m})$ for $n = 0$ to 4. Using (30) and integrating $a(h) = b(h)g(h)$ over category n with $dG = g dh$, we obtain the participation fraction from that category:

$$a_n = \frac{(G_n - G_{n-1})}{G^*} \left(2 - \frac{G_{n-1} + G_n}{G^*} \right), \quad (35)$$

where $G_n \equiv G(H_n) \leq G^*$. For $G_{n-1} < G^* < G_n$, (35) can be used with G^* substituted for G_n . For each category participating in ridging, ice is redistributed to other categories using (32) and (34). We rewrite (34) as $\gamma_n(h) = 1/[2(H^* - h_n)]$, where the continuous variable h_1 is replaced by the discrete h_n . For each h_n , ice is distributed to a range of thicknesses from $2h_n$ to $2\sqrt{H^*h_n}$. From (29) and (32), the ridging mode for category n is

$$w_r(n) = \frac{-a_n + \int_0^\infty a_n \gamma_n(h) dh}{N}. \quad (36)$$

The normalization factor required to satisfy (21) is

$$N = a_0 + \sum_{n=1}^{N_c} a_n \left(1 - \frac{1}{k_n} \right), \quad (37)$$

where $k_n = (h_{\max} + h_{\min})/(2h_n)$ is the ratio of the mean ridge thickness to the thickness of participating ice.

The ridging scheme is connected to the dynamics through the compressive ice strength P . From (12) and (27), P is equal to the energy dissipated per unit area of ridging and closing. *R75* proposed that P should be proportional to the gravitational work of ridge-building:

$$P = C_f C_p \int_0^\infty h^2 w_r dh, \quad (38)$$

where $C_p = \rho_i(\rho_w - \rho_i)\hat{g}/(2\rho_w)$, ρ_i is the ice density, ρ_w is the water density, and \hat{g} is the gravitational acceleration. The parameter C_f is the ratio of total energy sinks, including friction, to the gravitational sink. *R75* suggested $C_f = 2$, but numerical experiments by *Hopkins* [1994] give values in the range 10 to 17. *Flato and Hibler* [1995] chose $C_f = 17$ to maximize agreement with buoy velocities.

Combining (38) and (36), the ice strength is related to the ridging rate by

$$P = C_f C_p \frac{\sum_{n=1}^{N_c} [-a_n h_n^2 + \int_0^\infty a_n \gamma_n(h) h^2 dh]}{N}. \quad (39)$$

For $h_n \ll h_{\max}(n) = 2\sqrt{H^* h_n}$, the second term in brackets dominates the first term and is proportional to $h_n^{3/2}$. (The integral is proportional to h_{\max}^3 , and h_{\max} is proportional to $h_n^{1/2}$.) This scaling is consistent with *Hopkins* [1998], who used a 2D particle model to estimate ridge-building forces as a function of the thickness h and extent L of thin ice built into a ridge. He found that the average ridging force in kN/m is given approximately by

$$F = 7.3 h^{3/2} L^{1/2} \quad (40)$$

during the first stage of ridge-building, when the ridge sail is growing, and by

$$F = 95 h^{3/2} \quad (41)$$

during the second stage, when the ridge keel is broadening and deepening. Both (40) and (41) are consistent with the $h^{3/2}$ scaling of (39). For ridging of 1-m ice, the standard scheme (i.e., (34) and (39) with $H^* = 100$ m) gives a strength of about 100 kN/m, in good agreement with *Hopkins's* numerical experiments. For ridging ice 5 m thick, P is more than 1000 kN/m, which is larger than values inferred from stress measurements. *Richter-Menge and Elder* [1998] estimated that maximum wintertime ridge-building forces in the Beaufort Sea are of the order of 150 kN/m.

Instead of *R75*, many sea ice models use the strength parameterization of *H79*:

$$P = P^* h \exp(-CA_0), \quad (42)$$

where h is the mean ice thickness averaged over all categories (including open water), $C = 20$, and P^* is an empirical constant whose published values have ranged from 5000 N/m² [*H79*] to 27,500 N/m² [e.g., *Hibler and Walsh*, 1982]. This formula is less realistic than *R75* in several respects. First, it lacks a clear connection to the model energetics. Second, P as given by (42) depends only on the mean thickness and not on the amount of thin ice available for ridging. In reality, an ice pack with a mixture of thick and thin ice is likely to be weaker than a homogeneous

ice pack with the same mean thickness. Finally, P increases only linearly with thickness, instead of in proportion to $h^{3/2}$ as in *Hibler* [1980] and in the numerical experiments of *Hopkins* [1998].

The standard scheme satisfies several basic requirements of any ridging scheme in a multi-category sea ice model: Ice volume is conserved; thin ice ridges more readily than thick ice; and ice strength increases with ridge thickness. Also, the scheme has specific rules for computing participation, redistribution, and ice strength. On the other hand, the standard scheme is known to be inaccurate in some respects. For example, it does not account for void space of up to 30% in new ridges [*Lepparanta et al.*, 1995], and it generates ridges whose ITDs do not agree well with observations [e.g., *Babko et al.*, 2002; *Amundrud et al.*, 2004]. Other aspects of the standard scheme are uncertain; for instance, the parameters G^* , H^* , C_s , and C_f are not well constrained by data. Unfortunately, it is hard to evaluate ridging schemes based on comparisons to basin-scale observations, because the differences given by the choice of ridging scheme are small compared to other uncertainties. Ridging schemes are best validated by measuring ice concentration, thickness, strain rates, and stress at scales of 100 km or less. Stresses have been measured in the Arctic ice pack [e.g., *Richter-Menge and Elder*, 1998] and related to regional ice deformation [*Richter-Menge et al.*, 2002], but more observations and analysis are needed to evaluate ridging schemes in detail.

Another desired feature of ridging schemes is numerical robustness. As we show in the next section, the standard scheme can trigger oscillatory flow in high-resolution sea ice models. Thus the scheme may warrant changes not only to improve its empirical accuracy, but also to ensure that sea ice models run stably.

3. Numerical instability in a high-resolution sea ice model

For several years we have studied sea ice behavior in a high-resolution (9 km) regional model of the Arctic Ocean and peripheral seas [*Maslowski et al.*, 2004]. Previous results using both a basic sea ice model [*H79*] and CICE were reported in *Maslowski and Lipscomb* [2003]. The CICE simulations give better ice deformation fields than the basic model, thanks in part to the multi-category ITD and the more sophisticated treatment of ice strength and ridging. These simu-

lations are susceptible, however, to an undesirable and sometimes fatal numerical instability. The instability usually occurs near land, where strain rates are largest. Often it is triggered by strong winds that drive ice into or along a coast. It is characterized by checkerboard noise and unphysical values in the ice concentration, thickness, strength, velocity, shear, and divergence fields. Once the instability amplifies, the force balance is between the internal ice stress divergence, which generates excessive velocities, and the ocean drag, which opposes these velocities. Drag-limited model ice speeds are often in the range 1-3 m/s, an order of magnitude larger than observed speeds. In some cases the model crashes because the velocities violate the advective CFL limit. In other cases the model stabilizes within a few days or weeks after wind or ice conditions change, leaving behind a region of unphysically thick ice.

Here we show an example from a standalone simulation with CICE 3.1 on the 9-km pan-Arctic grid of *Maslowski et al.* [2004]. The surface temperature, specific humidity, and incoming solar and longwave radiation are from the ERA40 reanalysis [*Kållberg et al.*, 2004]. Surface winds are from the older ERA15 reanalysis [*Gibson et al.*, 1997], because the publicly available ERA40 winds were found to give unrealistic divergence at the North Pole. Ocean currents are set to zero, but the static ocean exerts a drag on moving ice. The key ridging parameters are $G^* = 0.15$, $H^* = 100$ m, $C_f = 17$, and $C_s = 0.25$. After a five-year spinup using a shorter time step to ensure stability, the standard simulation begins on 1 January 1979 with $\Delta t = 1$ hour. This is a typical time step for sea ice models, allowing the models to resolve diurnal changes in wind speed, air temperature, and incoming radiation.

The flow is well behaved until late June, when an instability develops near the Queen Elizabeth Islands in the Canadian Archipelago. Figure 1 shows snapshots of ice concentration, mean thickness, strength, and divergence in the unstable region on 2 July. Outside the unstable region, all fields are smooth with physically reasonable values: ice concentration of around 0.9, thickness of 3 – 5 m, strength of 10 – 30 kN/m, and divergence of no more than a few percent per day. In the unstable region, however, these fields are noisy and unrealistic. Ice concentrations range from 0.2 to 1.0, and thicknesses range from 1 m to 9 m. The maximum ice strength is nearly

2500 kN/m, and the maximum shear is an enormous 3500%/day. The instability persists for several weeks. The solid lines in Figure 2 show the maximum ice speed, mean thickness, internal ice stress divergence, and ridging rate during the first model year. (The entire grid is sampled once per day, and the maximum value is plotted.) The speed peaks at more than 2 m/s before settling down to realistic values in the fall. The maximum ice thickness increases to 30 m by late summer and then stabilizes but does not decrease. The internal stress gradient, which under stable conditions is less than 1 Pa, exceeds 10 Pa and dwarfs the other forces, except for the compensating ocean drag. The ridging rate, defined as the percentage of the ice area participating in ridging per day, also increases by an order of magnitude.

This behavior is unacceptable for climate simulations. It can crash the model and also can lead to excessive ice thickness near islands and coastlines. Because the instability is transient and not always fatal, it may go undetected in long simulations. Nor is it limited to grids that are typically considered high-resolution. For example, the CCSM sea ice model is usually run on a displaced-pole grid with nominal 1° resolution. Near Greenland, where meridians converge, grid cell edges are as small as 10 km, close to the threshold of instability with a 1-hour time step. Although CCSM is generally robust, the sea ice model can crash in certain configurations because of instability near the Greenland coast (Art Mirin, personal communication, 2006).

4. Instability in a one-dimensional test problem

The simulation described in section 3 is unstable in the sense that the energy can grow without bound (or until it is limited by the ocean drag). The instability is fundamentally numerical, not physical. The continuous equations have a physically realistic solution (i.e., realistic values of ice concentration, thickness, strength, and velocity), but the numerical solution can be inaccurate and potentially unstable if the time step is too long. The instability results from unstable feedback between the ridging scheme and the dynamics and is triggered by large increases in ice strength between one time step and the next. *Hutchings* [2004] described this instability in a model that has a single ice thickness category and uses the *H79* strength parameterization. Instability is triggered more easily in multi-category models with ridging schemes based on *T75* and *R75*.

The instability can be explained in terms of a simple 1D test problem. Assume that the flow is in the x direction, with $v = 0$ and no variation in the y direction. (This case is analyzed in *Gray* [1999].) The strain rates in (7)–(9) are

$$D_D = D_T = \frac{\partial u}{\partial x} \equiv D, \quad D_S = 0, \quad (43)$$

which imply

$$\Delta = |D| \sqrt{1 + 1/e^2}. \quad (44)$$

From (6), the VP equations for the stresses are

$$\hat{\sigma}_1 = 2\zeta D - P, \quad \hat{\sigma}_2 = 2\eta D, \quad \hat{\sigma}_{12} = 0, \quad (45)$$

which can be rewritten using (10) and (44) as

$$\hat{\sigma}_1 = P \left(\frac{D}{\alpha |D|} - 1 \right), \quad \hat{\sigma}_2 = \frac{PD}{\alpha e^2 |D|}, \quad \hat{\sigma}_{12} = 0, \quad (46)$$

where $e = 2$ and $\alpha \equiv \sqrt{1 + 1/e^2} \cong 1.12$ for the standard yield curve. Using (4) and noting that $\sigma_{11} = (\hat{\sigma}_1 + \hat{\sigma}_2)/2$, the x component of the stress gradient can be written as

$$F_x = \frac{\partial \sigma_{11}}{\partial x} = \frac{1}{2} \frac{\partial}{\partial x} \left[P \left(\alpha \frac{D}{|D|} - 1 \right) \right]. \quad (47)$$

Thus the direction and magnitude of F_x depend on the sign of D :

$$F_x = \frac{-(\alpha + 1)}{2} \frac{\partial P}{\partial x}, \quad D < 0, \quad (48)$$

$$F_x = \frac{(\alpha - 1)}{2} \frac{\partial P}{\partial x}, \quad D > 0. \quad (49)$$

Under convergence ($D < 0$), F_x is directed opposite the strength gradient with a magnitude slightly greater than $|\partial P / \partial x|$. Under divergence ($D > 0$), F_x has the same sign as $\partial P / \partial x$ but is about ten times smaller in magnitude. VP models avoid the discontinuity at $D = 0$ by limiting the viscosities (or equivalently, by holding Δ in (11) to a prescribed minimum). As a result, the flow is viscous rather than plastic at very small strain rates.

The initial and boundary conditions for the test problem are as follows. The east and west boundaries are closed, with $u = 0$ at the boundaries, and the north and south boundaries are open and periodic, precluding any variation in the y direction. There is a uniform wind from the west with speed 10 m/s. (Arctic surface winds are typically of the order of 5 m/s, but occasionally reach 10–20 m/s.) The wind stress is given by

$$\tau_x = c_a \rho_a |\mathbf{u}_a| u_a, \quad \tau_y = c_a \rho_a |\mathbf{u}_a| v_a, \quad (50)$$

where $\mathbf{u}_a = (u_a, v_a)$ is the wind speed, $c_a = 0.0012$ is an air drag coefficient, and $\rho_a = 1.25 \text{ kg/m}^3$ is the air density. For the prescribed westerly wind, (50) gives $\tau_x = 0.15 \text{ N/m}^2$ and $\tau_y = 0$. The ocean is an inert slab that exerts a drag on moving ice, and the Coriolis force and sea surface tilt are set to zero. Transport and ridging are included, but thermodynamic processes are not. The basic ridging parameters are $G^* = 0.15$, $H^* = 100 \text{ m}$, $C_f = 17$, and $C_s = 0.25$.

The ice pack is initialized with one of the following three thickness distributions. For ITD1, which represents typical multiyear ice in the wintertime Arctic, the ice fractions in the five categories are (0.05, 0.10, 0.30, 0.35, 0.20), with no open water, giving a mean thickness of 2.73 m. For ITD2 the initial ice is 5 m thick, again with no open water. This distribution represents thick, heavily ridged ice, as may occur north of Greenland and Canada where the pack is converging. ITD3 is like ITD2, except that 20% of the ice is replaced by open water. This kind of distribution occurs occasionally when rapid divergence follows a period of convergence and ridging, or when the thin part of the ITD melts in summer, leaving behind only thick ice. ITD3 is typical of regions where instabilities arise in realistic simulations. The initial strengths for these three ITDs are 59 kN/m, 1279 kN/m, and zero, respectively.

The resulting flow pattern is straightforward. With the westerly wind piling up ice at the eastern boundary, $u \geq 0$ and $D \leq 0$ everywhere. Using (48), the momentum equation can be written as

$$m \frac{\partial u}{\partial t} = \tau_x - c_w u - \frac{(\alpha + 1)}{2} \frac{\partial P}{\partial x}, \quad (51)$$

where c_w is an ocean drag coefficient. (In CICE the ocean drag depends quadratically on the ice speed, but this point is inessential to the argument.) Far from the eastern boundary, the flow is in free drift with $\partial P/\partial x = 0$ and $u = 0.17$ m/s. Near the boundary, the strength increases under convergence, giving $\partial P/\partial x > 0$. Thus the ice stress gradient combines with the ocean drag to oppose the wind stress. If the acceleration is small compared to the forcing terms, as usually assumed in sea ice models, the velocity is

$$u = \frac{1}{c_w} \left[\tau_x - \frac{(\alpha + 1)}{2} \frac{\partial P}{\partial x} \right]. \quad (52)$$

As $\partial P/\partial x$ increases, u decreases until the flow becomes slow and viscous. In steady state, P increases linearly from west to east, balancing the wind stress, and u is close to zero everywhere.

This problem is discretized on a regular square grid with 100 cells in the east-west direction. (The number of cells in the north-south direction is unimportant since there is no y variation.) Each cell is 10 km on a side, which is close to the finest resolution in current global and pan-Arctic models. The equations are discretized on the B-grid, with strength and internal stress at cell centers and velocity at cell corners. The strength gradient $\partial P/\partial x$ is located at cell corners and is discretized for corner i as $(P_{i+1}^n - P_i^n)/\Delta x$, where i is the zonal index and n is the time index. (We omit the meridional index j .) Suppose the model is initialized with ITD1 and run for 30 days with $\Delta t = 300$ s. Figure 3 shows profiles of u and P after 1, 5, and 30 days. By day 30 the strength is close to 200 kN/m near the eastern boundary, and the strength gradient is smooth and not too steep. The flow has almost stopped, with the wind stress balanced by $\partial P/\partial x$ over most of the grid. With smaller Δt or Δx the results are nearly unchanged, showing that the model solution converges.

If Δt is larger, then P can increase substantially between time levels n and $n + 1$. Since the stresses are functions of P^n , the solution loses accuracy. Consider two neighboring grid cells i and $i + 1$, with cell $i + 1$ immediately adjacent to the eastern boundary. In the continuous solution, the cell interface velocity $u_i \geq 0$ and the boundary velocity $u_{i+1} = 0$ for all time. Suppose the strength gradient $(P_{i+1} - P_i)/\Delta x$ is small at time level $n - 1$, so that ice converges in cell

$i + 1$, giving $P_{i+1}^n \gg P_i^n$. If Δt is large enough, the magnitude of the internal stress force at time n can exceed that of the wind stress:

$$\tau_x - \frac{(\alpha + 1)}{2} \frac{P_{i+1}^n - P_i^n}{\Delta x} < 0. \quad (53)$$

Then (52) implies that $u_i^{n+1} < 0$; i.e., the flow must change direction. If the flow reverses, however, the divergence $D_{i+1} > 0$, and F_x is no longer given everywhere by (48). Instead, (47) gives

$$F_x = \frac{1}{2\Delta x} [(\alpha - 1)P_{i+1} + (\alpha + 1)P_i], \quad (54)$$

which must be positive (since $P_i \geq 0$ for all i and $\alpha > 1$) and thus in the same direction as the wind stress. But if F_x and τ_x have the same sign, the flow cannot reverse. In other words, there is no consistent numerical solution for u_i^{n+1} under plastic flow. The only consistent numerical solution is viscous creep, which in general is a poor approximation to the true solution. (Here we distinguish between the true solution of the continuous equations, in which the flow is convergent and stable, and the numerical solution, in which P is inaccurate and the flow must compensate in an unphysical way.)

The resulting flow depends to some extent on the solution method. Any scheme, however, will give inaccurate solutions once the ice strength overshoots its true value. In the standard EVP scheme the stresses and velocities are subcycled 120 times per time step, and elastic waves are damped on a time scale $T = 0.36\Delta t$, which gives excellent accuracy and stability under most conditions [Hunke, 2001]. When applied with a long time step in the situation described above, the EVP solution for u_i^{n+1} does not converge to the (inaccurate) viscous solution, but instead is large and negative. As a result, ice flows from cell $i + 1$ back to cell i , decreasing and possibly reversing the stress gradient. Over the next few time steps, u and P can oscillate, and the oscillations can spread to neighboring grid cells. Two outcomes are possible. If Δt is not too long, the oscillations damp out and convergent flow is restored, more or less in agreement with the true solution. But if Δt is long enough, the oscillations grow until the velocities and strength gradients become large and unphysical, as in section 3.

Instability is triggered easily when the ice pack is initialized with ITD3 (5-m ice with 20% open water). At first the ice is in free drift, because it has no strength when the open water fraction $A_0 \geq G^*$. In the region of convergence near the eastern boundary, A_0 soon falls below G^* and the ice acquires strength, resisting the wind stress and slowing the flow. Figure 4 shows profiles of P and u after 1 day and 5 days with three values of Δt . With $\Delta t = 5$ minutes the strength and velocity fields remain smooth and monotonic. With $\Delta t = 30$ minutes these fields have unphysical oscillations after day 1, but the oscillations have mostly damped out by day 5. With $\Delta t = 60$ minutes the oscillations persist; by the end of day 5, the maximum speed is 1.21 m/s and the largest strength is 2120 kN/m. These values (off the scale of the figure) are too large by an order of magnitude.

Figure 5 shows how the mean kinetic energy per grid cell (in J/m^2) evolves for various values of Δt with the three ITDs. Each simulation is run for 30 days or until the model crashes with an advective CFL violation. For stable runs, the kinetic energy decreases monotonically. The most stable configuration is ITD1 (Figure 5a) which permits a time step of nearly 3 hours. ITD2 (Figure 5b) is less stable; the model crashes for Δt greater than about 90 minutes. There is a range of time steps for which the strength and velocity are noisy but bounded. With $\Delta t = 60$ minutes, for example, the energy declines gradually for 10 days, then increases for several days before leveling out. By the end of the run, the maximum internal stress gradients are ~ 1 Pa, several times larger than the wind stress. The mean open water fraction is about 0.9, and P has dropped from ~ 1000 kN/m to ~ 200 kN/m. In a given grid cell, P can change by ~ 50 kN/m from one time step to the next, giving noisy velocities and large strain rates. If the model were run with active thermodynamics and winter temperatures, there would be excessive ice growth in leads because of numerically generated opening and closing. ITD3 (Figure 5c) is the least stable ITD because it is conducive to sudden large changes in P . The model is well-behaved for small Δt (< 20 minutes), noisy for intermediate values (~ 40 minutes), and unstable for larger values (> 60 minutes).

To confirm that the instability is not unique to a particular solution scheme, we ran several experiments with modified dynamics. First we increased the number of EVP subcycles from 120 to 1200. This change makes the model more stable by damping out large velocities and approaching the viscous solution. However, the damping is achieved at considerable computational cost, without much improvement in accuracy. Next, we varied the yield-curve parameter e , which determines the relative sizes of compressive and shear stresses. Neither an increase nor a decrease in e improves the stability. Third, we replaced the elliptical yield curve with a teardrop yield curve, as described by *Zhang and Rothrock* [2005]:

$$\frac{\sigma_{II}}{P} = -\frac{\sigma_I}{P} \left(1 + \frac{\sigma_I}{P}\right)^{1/2}, \quad (55)$$

where $\sigma_I = (\sigma_1 + \sigma_2)/2$ and $\sigma_{II} = (\sigma_1 - \sigma_2)/2$. This yield curve is confined to the third quadrant of principal stress space and therefore permits no tensile stresses under uniaxial divergence [*Gray*, 1999]. The teardrop curve, however, is no more stable than the elliptical curve for the 1D test problem.

Finally, we implemented the alternating direction implicit (ADI) solver of *Zhang and Rothrock* [2000]. The ADI scheme gives an efficient solution to the VP equations (without elastic waves) by decoupling the u and v momentum equations and solving each equation with two passes of a tridiagonal matrix solver. *Zhang and Rothrock* [2000] found that the method is more accurate if each time step is broken into 5-15 pseudo time steps, with the viscosities, but not the ice strength, updated after each pseudo step. Either with or without pseudo steps, the ADI solver is no more stable or accurate than the EVP solver. Qualitatively, the behavior is similar to that given by the EVP scheme, with large oscillations in u and P . Other implicit methods such as the line successive relaxation solver of *Zhang and Hibler* [1997] might be more stable than ADI, but the solutions would still be inaccurate.

Another approach is to change the time discretization of P . Since large strength changes on short time scales lead to instability, it would be natural to treat P semi-implicitly or implicitly. *Hutchings* [2004] describes such a scheme for models in which the strength can be expressed as a

function of the total ice mass per unit area. Although this scheme cannot be applied in CICE, we did try updating P at regular intervals during the EVP subcycling. This approach, unfortunately, does not stabilize the scheme, because frequent updating of P excites elastic waves and does not allow the EVP solution to converge. We also tried a predictor-corrector method, running the EVP solver a second time during each time step with the average of P^n and the predicted P^{n+1} . This method does not work either, because the change in P is so nonlinear that the average of P^n and the predicted P^{n+1} can be less accurate than P^n itself.

Stability can be improved by artificially reducing the rate of change of P . Suppose P is updated as follows:

$$P^{n+1} = P^n + (P^* - P^n) \frac{\Delta t_P}{\Delta t}, \quad (56)$$

where P^* is the predicted value of P^{n+1} following dynamics and ridging, and $\Delta t_P < \Delta t$ is a time scale that controls the rate of relaxation to the predicted value. The smaller the value of Δt_P , the slower the relaxation and the longer the allowable Δt . With $\Delta t_P = 10$ minutes, for example, the model is stable for ITD3 with a time step of several hours. This change, however, is not very satisfactory. The ice strength is lagged in time everywhere, whereas large strength gradients are usually confined to a few grid cells at certain times of year.

In summary, sea ice models using the standard ridging scheme and VP or EVP dynamics at a resolution of ~ 10 km are unstable with a time step of ~ 30 minutes or more. The instability arises because for some ITDs, the ice strength (and its gradient) can change substantially in less than an hour. As a result, the internal stress forces can exceed the external driving forces, leading to oscillations in the strength and velocity fields. The instability is independent of details such as the shape of the yield curve and the form of the stress equations (VP or EVP).

If P were a well understood and easily measurable physical property, like pressure in the atmosphere or ocean, the best solution probably would be to decrease Δt and pay the added computational cost. But P is derived from a ridging scheme with many uncertainties. Thus the time scale for instability is not necessarily physical, but could be an unforeseen result of unverified

assumptions about ridging. In the next section we show that stability can be improved by physically reasonable changes in the ridging parameterization.

5. Improving model stability

We now test the effects of various ridging changes on model stability. Since the 1D problem is somewhat artificial, we introduce a complementary test problem in two dimensions. This problem has open boundaries, island topography, strong shear, and a non-zero steady-state solution. Although 2D flow is more complex than 1D flow, the mechanism for instability is the same: Abrupt changes in $\partial P / \partial x$ lead to internal stresses that exceed the external forcing, and the resulting flow is noisy and potentially unstable.

For the 2D test case, CICE is run on a regular 100×100 grid with 10-km resolution. Both the north-south and east-west boundaries are open and periodic. In the center of the grid is an L-shaped island whose legs are 200 km in length and 50 km in width, rotated so that the legs open toward the southwest. The ice is forced with a uniform southwesterly wind with components $u = v = 10$ m/s, giving an ice speed of 14.1 m/s. Initial conditions and forcing are otherwise the same as in the 1D problem. Without the island, the steady-state flow would be to the northeast at 0.23 m/s. At that speed, Δt could be up to 17 hours without violating the advective CFL limit.

With standard ridging parameters and with the initial ITDs from section 3, the model is roughly as unstable for the 2D test problem as for the 1D problem. Figure 6a and 6b show the fractional ice area and divergence, respectively, after day 1 of an ITD3 simulation with $\Delta t = 30$ minutes. Unstable flow develops upwind of the island where the pack converges and soon spreads over a large region.

In the following sections we test several ridging changes using the 1D and 2D test problems. For each ITD the model is run for 30 days with various time steps. Beginning with a stable run, Δt is increased in increments of 5 minutes until the model becomes unstable. A run is deemed unstable if the maximum ice speed exceeds 0.5 m/s at any time or if the model crashes with an advective CFL violation. Ice speeds greater than 0.5 m/s cannot be driven by the wind stress and

invariably are associated with numerical instability. Other stability criteria (based on mean kinetic energy, for example) were found to give similar results.

5.1. The ridging participation function

The least stable initial condition for both test problems is ITD3, for which the ice strength increases sharply as the open water fraction A_0 is reduced. In the standard ridging scheme the fractional participation in ridging by ice of thickness h is $a(h) = b(h)g(h)$, where $b(h)$ is a linear weighting function given by (30). We will refer to this participation function as P0. Only the thin part of the ITD with $G(h) < G^*$ participates in ridging and contributes to the strength. The strength is zero when $A_0 > G^*$ but can be relatively large when A_0 is slightly less than G^* . Thus large strength gradients can arise between neighboring grid cells with small differences in A_0 .

There is no obvious physical reason that the ice strength should vanish at a particular value of A_0 . We are therefore motivated to introduce a participation function $b(h)$ that decreases smoothly with the open water fraction, without a cutoff value G^* . Our first candidate function, denoted by P1, falls off exponentially with $G(h)$:

$$b(h) = \frac{\exp[-G(h)/a^*]}{a^*[1 - \exp(-1/a^*)]}, \quad (57)$$

where a^* is an empirical parameter that replaces G^* , and the denominator is a normalizing factor. Integrating $a(h) = b(h)g(h)$ between category boundaries H_{n-1} and H_n gives the fractional participation for category n :

$$a_n = \frac{\exp[-G_n/a^*] - \exp[-G_{n-1}/a^*]}{1 - \exp(-1/a^*)}. \quad (58)$$

From (57) the mean value of G for ice participating in ridging is a^* , as compared to $G^*/3$ for the standard scheme. Thus, setting $a^* = 0.05$ gives the same mean G as does the standard scheme with $G^* = 0.15$. Henceforth we assume $a^* = 0.05$ unless stated otherwise.

Although (57) allows all ice of all thicknesses to participate in ridging, the participation of ice in the thick part of the ITD is very small. For ITD1, P0 gives participation fractions $a_n = (0.63, 0.32, 0.05, 1.2 \times 10^{-4}, 1.1 \times 10^{-7})$ in the respective categories, as compared to $(0.56, 0.44, 0, 0, 0)$

for P0. The ice strengths are nearly identical: 59 kN/m for P0 and 60 kN/m for P1. This agreement is somewhat fortuitous. Relative to P0, the function P1 favors participation by the thinnest part of the ITD ($G(h) < 0.03$) and by ice with $G(h) > G^*$. As a result, the strengths can differ by ~ 10 -20 kN/m. With ITD3, for example, P1 gives $P = 19$ kN/m and P0 gives $P = 0$.

A possible objection to (57) is that it allows ridging to occur for large values of A_0 (i.e., $A_0 > 0.15$). Ridging in the presence of open water can be reduced, though not eliminated, by decreasing a^* . For ITD3, changing a^* from 0.05 to 0.03 reduces the participation of 5-m ice from 0.018 to 0.001, giving an ice strength of only 1.3 kN/m. A smaller a^* generally implies weaker ice; the strength of ITD1 with $a^* = 0.03$ is 36 kN/m, compared to 60 kN/m with $a^* = 0.05$.

Another candidate participation function, denoted by P2, is obtained by making $b(h)$ proportional to $1/h^2$. Amundrud *et al.* [2004] suggested such a function, based on the fact that the buckling strength of a floating plate is proportional to the square of its thickness. The singularity at $h = 0$ can be avoided by adding a term in the denominator:

$$b(h) \propto \frac{1}{(h + h_{\text{eff}})^2}, \quad (59)$$

where h_{eff} is the effective thickness of very thin ice or open water. Here we set $h_{\text{eff}} = 0.2$ m, which makes it four times more likely (per unit area of coverage) that open water will close than that 20-cm ice will ridge. Function P2, like P1, maintains a finite ice strength as A_0 increases. Relative to P0 and P1, function P2 usually enhances the participation of thick ice. With ITD1, for example, P2 yields participation fractions of (0.53, 0.18, 0.17, 0.09, 0.02) in the respective ice categories. The strength P is 151 kN/m, more than double the values given by P0 and P1. For ITD3, however, P2 gives a strength of just 6 kN/m, as opposed to 19 kN/m for P1, because the participation per unit area of 5-m ice is about 700 times less than that of open water.

We now compare functions P1 and P2 to the standard function P0, with $a^* = 0.05$ in (57) and $h_{\text{eff}} = 0.2$ m in (59). Table 1 shows how the maximum stable time step varies with different ridging assumptions and ITDs for the 1D test problem, and Table 2 gives the same information for

the 2D problem. The first three rows give results for P0, P1, and P2, respectively. (The other rows are discussed in section 5.2.)

For the standard function P0, the least stable initial condition is ITD3, which allows a maximum time step of only 25 minutes for the 1D problem and 20 minutes for the 2D problem. This is consistent with the results shown in Figures 4, 5, and 6. Convergence upwind of topography quickly reduces the open water fraction A_0 to 0.15 or less, giving large ice strength gradients and promoting oscillatory flow. With ITD2, P0 is somewhat more stable; Δt is limited to 90 minutes for the 1D case and 55 minutes for the 2D case. The ITD1 simulation is relatively stable, with a maximum Δt of more than 2 hours.

The exponential function P1 is the most stable of the three functions. For the 1D case the maximum stable time steps are 115 minutes for ITD2, 155 minutes for ITD3, and 225 minutes for ITD1. For the 2D case the limiting steps for all three ITDs are at least 4 hours, suggesting that the flow is more stable under a combination of convergence and shear than under pure convergence. If a^* is reduced to 0.03 (results not shown), the maximum stable times steps for ITD2 and ITD3 fall to 85 minutes and 115 minutes, respectively, for the 1D problem.

P1 is relatively stable for ITD3 because the strength varies smoothly for A_0 in the range 0.1 to 0.2. Figures 6c and 6d show the ice area and divergence for an ITD3 simulation identical to that shown in Figures 6a and 6b, except that P0 is replaced by P1. Divergence is large in the lee of the island, but the flow remains smooth and stable. The ice strength varies more rapidly with A_0 when the ice is compact than when $A_0 > 0.1$. With 5-m ice, for example, P increases from 143 kN/m with $A_0 = 0.10$ to 1279 kN/m when $A_0 = 0$. For this reason the largest strength gradients and least stable flows are associated with the thick, compact ice of ITD2.

P2, like P1, is relatively stable when $A_0 > 0.1$. The ice strengthens only slightly, from 6 kN/m to 14 kN/m, as A_0 decreases from 0.20 to 0.10. But when the ice is compact, P is very sensitive to the open water fraction, increasing from 135 kN/m to 1279 kN/m as A_0 falls from 0.01 to zero. For this reason P2 is highly unstable for ITD2. In the 2D test case, divergence downwind of the island reduces the strength by an order of magnitude or more, promoting oscilla-

tions. The maximum Δt for ITD2 is only 25 minutes for the 2D case, as compared to 40 minutes for the 1D case with pure convergence.

P2 can be made more stable by increasing h_{eff} . With ITD2, for example, the maximum stable time step doubles, from 25 minutes to 50 minutes, when h_{eff} is increased from 0.2 m to 0.3 m. However, this change further increases participation by thick ice, which is already high. For ITD1, P increases to 174 kN/m, nearly three times the values given by P0 and P1, with more than one-third of the participation from ice in categories 3, 4, and 5 (i.e., thicker than 1.4 m).

These results suggest that the exponential function P1 is the best of the three participation functions. At 10-km resolution, P1 allows a maximum time step of about 2 hours or more for a variety of thickness distributions and flow patterns. Moreover, P0 and P1 imply similar ice strengths for typical ITDs. To the extent that the P0 strengths are accurate (or to the extent that models have been tuned for P0), P1 is likely to give similar results.

This hypothesis is confirmed by the pan-Arctic model. Figure 7 shows results from a simulation using P1, but otherwise the same as that of Figure 1. The ice concentration, thickness, strength, and divergence fields are shown for 2 July 1979 in the region that is unstable in the standard run. All fields are smooth and realistic. In Figure 2 the dashed lines show the maximum values of ice thickness, speed, internal stress divergence, and ridging rate from the P1 simulation. These fields have no large oscillations, showing that the flow is stable throughout the year. During periods when both runs are stable, the maxima from the two simulations are nearly identical. After one year the ice thickness fields from the two runs are very similar except in the region of instability, where thick ice lingers. In the central Arctic, ice in the P1 simulation is generally weaker by 10-20 kN/m, because P1 ridges more ice in category 1 ($h < 0.6$ m) and less in category 2 ($0.6 \text{ m} < h < 1.4$ m). The ice velocities differ by less than 0.01 m/s almost everywhere.

P1 promotes stability by increasing the time scale for large changes in P . (A large change can be defined as a change that yields internal ice forces comparable to or greater than the driving forces.) It is possible that large strength changes do, in fact, occur on time scales of a fraction of an hour at the 10-km scale. If this is true, then P1 could make the model less accurate. However,

ITDs with fast-changing strengths are relatively rare, suggesting that the loss of accuracy would be small compared to other model uncertainties.

The value of a^* is uncertain. Setting $a^* = 0.05$ optimizes agreement with P0 but may allow too much ridging when the open water fraction is large (i.e., 0.1 to 0.2). Ideally, a^* would be determined empirically based on measurements of opening and closing of open water, along with ridging in various thickness categories. The required deformation fields could be derived from synthetic aperture radar (SAR) imagery [e.g., *Kwok and Cunningham, 2002*]. Ice thickness could be estimated from SAR imagery (with the help of a numerical model) or measured in situ.

5.2. The ridging redistribution function

The standard scheme with $H^* = 100$ m creates relatively thick ridges with large potential energy. Reducing H^* to give shallower ridges could improve stability by lowering the large ice strengths that lead to oscillating velocities. Such a change would also improve agreement with observations, which show that ridges produced by the standard scheme are too thick. *Amundrud et al. [2004]* used first-year ice draft measurements to show that the standard scheme with $H^* = 100$ m creates too little ice in the 3 – 5 m range and too much ice thicker than 10 m. Some ridge keels do reach the maximum thickness of $20h_1^{1/2}$ implied by the standard scheme (where h_1 is the thickness of ridging ice), but most do not, possibly because most ridging ice floes are too narrow to form ridges of maximum thickness. The relationship $h_{\max} \cong 15h_1^{1/2}$, or $H^* \cong 50$ m, gives a better fit to the data (Figure 5 of their paper). CICE has typically been run with $H^* = 25$ m, a value that is probably too small for first-year ridges but may be appropriate for consolidated multiyear ridges. *Flato and Hibler [1995]* found that this value gives excessive ice speeds. Ice speeds can be reduced, however, by tuning other parameters such as the wind and ocean drag coefficients.

Agreement with observations can be improved further by changing the shape of the redistribution function γ . Ice draft measurements from upward-looking sonar show that $g(h)$ in the central Arctic for $h > 5$ m is fit very well by a negative exponential with an e -folding scale of about 3 m

(Vinje *et al.*, 1998; NSIDC, 2005). Amundrud *et al.* [2004] found that the ITDs of first-year ridges are well approximated by a truncated exponential:

$$\gamma(h) = \gamma_0 \exp(-h/\lambda), \quad h \leq h_{\max}, \quad (60)$$

where $\lambda = 6$ m is an empirical e -folding scale, γ_0 is a normalization factor, and h_{\max} is computed using an empirical floe size distribution. Here we take a simpler approach without a cutoff thickness h_{\max} . We assume that the ITD of ridges built from ice of thickness h_n is given by

$$\gamma_n(h) = \gamma_{0n} \exp[-(h - h_{\min})/\lambda], \quad (61)$$

for $h \geq h_{\min}$, with $\gamma_n(h) = 0$ for $h < h_{\min}$. We set $h_{\min} = \min(2h_n, h_n + h_{\text{raft}})$ with $h_{\text{raft}} = 1$ m, as for the uniform ITD. The normalization factor is $\gamma_{0n} = 1/(k_n \lambda)$, where $k_n = (h_{\min} + \lambda)/h_n$ is the ratio of the mean ridge thickness to the thickness of ridging ice. The e -folding scale is given by

$$\lambda = \mu h_n^{1/2}, \quad (62)$$

where μ is a tunable parameter with units of $\text{m}^{1/2}$. Thus the mean ridge thickness increases in proportion to $h_n^{1/2}$, in agreement with Hibler [1980]. Setting $\mu = 3.0, 4.0, 5.0$, or $6.0 \text{ m}^{1/2}$ gives ice of about the same strength as does setting $H^* = 25, 50, 75$, or 100 m, respectively, in the standard scheme. With $\mu = 4.0$, the e -folding scale λ lies in the range 1 to 4 m for most ridging ice (i.e. for $0.05 \text{ m} < h_n < 1 \text{ m}$). As shown in Figure 8, this range is consistent with ITDs along submarine tracks in the central Arctic [NSIDC, 2005]. It is worth noting that a ridge with an exponential ITD has about 50% more potential energy per unit area than does a ridge of the same mean thickness \bar{h} with a uniform ITD. In the limit of small h_n , an exponential ridge described by (61) has a mean square thickness $2\bar{h}^2$, as opposed to $(4/3)\bar{h}^2$ for a standard ridge given by (34).

We now show how model stability depends on the redistribution function. R0 denotes the standard uniform ridge ITD with $H^* = 100$ m; R1 denotes a uniform ITD with $H^* = 25$ m; and R2 refers to an exponential ITD with $\mu = 4.0$. Compared to R0, function R1 decreases the initial ice strength by about factor of two: from 59 kN/m to 30 kN/m for ITD1, and from 1279 kN/m to 674 kN/m for ITD2. R2 gives intermediate strengths: 39 kN/m for ITD1 and

933 m for ITD2. Tables 1 and 2 show the stability limits for the two test cases. Rows 4 and 5 of the tables give results for R1 and R2, respectively, when used with the standard participation function P0. Rows 6 and 7 show results for R1 and R2 combined with the more stable P1.

When combined with P0, functions R1 and R2 modestly improve stability. The improvements resulting from reduced ice strength are partly offset by the larger strain rates associated with weaker ice. With ITD3, function R1 increases the minimum time step from 25 to 50 minutes for the 1D test case, and from 20 to 30 minutes for the 2D case. ITD2 also becomes more stable, with Δt increasing from 90 to 135 minutes for the 1D case and from 55 to 85 minutes for the 2D case. The gains are smaller for R2, because the ice strength does not decrease as much. For the 1D case, R2 increases the limiting Δt for ITD2 from 90 to 120 minutes, and the maximum step for ITD3 is unchanged. The results for a uniform ITD with $H^* = 50$ m (not shown) are similar to those for R2, because the ice strengths are about the same.

When R1 and R2 are combined with the exponential P1, stability again improves modestly. These results (rows 6 and 7) should be compared to row 2, which gives results for P1 combined with R0. For P1/R0, the least stable simulation is the 1D run with ITD2, for which the maximum Δt is 115 minutes. For the P1/R1 combination, the stability limit is 145 minutes (with ITD3), and for P1/R2, the limit is 150 minutes (with ITD2). Thus, for the least stable cases, the maximum stable time step increases by about 25% with either R1 or R2. For the 2D test case, the runs with P1/R0 are already quite stable, and the improvements given by R1 and R2 are negligible.

When R2 is substituted for R0 in the pan-Arctic simulation of section 3, the changes are fairly small. Ice in the central Arctic is weaker by 5 to 15 kN/m because ridges are thinner. Ice velocities change by less than 0.01 m/s except near topography, where the difference can approach 0.02 m/s. The ice thickness fields after one year agree to within 0.1 m in the central Arctic and to within ~ 0.5 m near coastlines.

In summary, the redistribution functions R1 and R2 improve stability, but not nearly as much as the participation function P1. The main reason to change the redistribution is to improve agreement with observations of ridged ice. By construction, the exponential function R2 gives the

most accurate ridge ITDs. Function R2 with $\mu = 4.0$ creates ridges that are about as thick, on average, as those given by a uniform ITD with $H^* = 25$ m, but are as strong as those given by a uniform ITD with $H^* = 50$ m. Differences in ridged ice distribution between R2 and R0 are barely resolved in a five-category model, but would be noticeable in a model with 10 or more categories. More importantly, accurate ridge ITDs are more likely to give the right ice strength for the right reasons.

5.3. Ice strength

Until now, we have assumed that the ice strength is proportional to the potential energy of ridges, as in *R75*. For reasons given in section 2, this assumption is more realistic than the simpler *H79* strength parameterization (42). Equation (42), however, yields very stable ice. The exponential term ensures that the ice strength varies smoothly with the open water fraction, as for participation function P1. Also, the linear scaling of ice strength with mean thickness gives maximum strengths of ~ 100 kN/m or less for multiyear ice. Thus the strength gradients seldom become large enough to promote instability. For both test cases (with $P^* = 20,000$ N/m², $C = 20$, and otherwise standard parameters), the maximum stable time step is at least 6 hours for all three ITDs. Because of its stability, the *H79* strength formula is used in the sea ice component of the Hadley Centre climate model, HadGEM1 [McLaren *et al.*, 2005], which is unstable with the *R75* formulation. The HadGEM1 sea ice model is run on a 1° latitude-longitude grid with very fine zonal resolution near the North Pole.)

For thick ice, the *H79* formula gives strengths much less than the *R75* strengths. As a result, the ice pack can converge excessively. When (42) is used in the 2D test case with ITD2, the mean ice thickness in some grid cells is more than 10 m after just two model days. The thickness eventually stabilizes at 18 m, when the strength is sufficient (~ 350 kN/m) to resist further convergence. In reality, the mean Arctic ice thickness rarely exceeds 5–6 m on scales of several kilometers. Thus, excessive ice thicknesses in models using the *H79* strength formula are more likely the result of weak ice than of numerical instability.

Although the *R75* formulation is more realistic than that of *H79*, it has become less compelling with the realization that most of the energy sinks under shear and convergence are not gravitational but frictional [e.g., *Hopkins*, 1994]. *R75* proposed that frictional sinks, like gravitational sinks, scale with the square of the ridge thickness. He did not consider sliding friction (i.e., friction between floe edges, not associated with ridging), which is thought to scale linearly with thickness. *Wilchinsky and Feltham* [2004b], building on studies by *Ukita and Moritz* [2000], argued that the sliding contribution is relatively more important for thin ice than for thick ice. Thus the ratio of frictional work to gravitational work, parameterized by the factor C_f , may decrease with thickness. This is consistent with numerical simulations by *Hopkins* [1998], who found that the lowest values, $C_f \approx 10$, are associated with the thickest lead ice, $h = 1$ m. It is likely that C_f for thicker ice would be smaller still. *Wilchinsky and Feltham* [2004b] therefore suggested parameterizing the ice strength as the sum of a potential energy term and a sliding friction term. This change would tend to enhance stability, provided that the work done by sliding friction increases more slowly with thickness than does the gravitational work. A model of sliding friction, however, is beyond the scope of this paper.

6. Discussion and conclusions

We have shown that a feedback between the standard ridging scheme and VP or EVP dynamics can cause instability in high-resolution (~ 10 km) sea ice models, reducing the maximum stable time step to 30 minutes or less. The instability is triggered by abrupt changes in the ice strength P , resulting in excessive internal stress gradients and oscillatory flow. The resulting fields of ice concentration, thickness, strength, velocity and strain rates are noisy and unrealistic. Unstable flow typically arises near islands and coastlines where convergence and shear are large. Thickness distributions with a mixture of thick ice and 10–20% open water are especially prone to instability. The instability is made possible by the large changes in ice stress that occur as the flow switches between convergence and divergence in the VP model. However, the instability is fundamentally numerical, not physical. The model gives realistic behavior with small Δt , becoming unstable only when Δt exceeds the time scale for large changes in P .

It is useful to distinguish between two senses in which a sea ice dynamics model can be unstable [Pritchard, 2005]: (1) The solutions are sensitive to small changes in the initial conditions, or (2) The energy can grow without bound. This paper is concerned with instability in the second sense. Gray and Killworth [1995] and Gray [1999] showed that under uniaxial divergence, the standard VP equations (in their continuous form) are unstable in the first sense. The instability results from the passage of the elliptical yield curve through the second and fourth quadrants of principal stress space, giving rise to tensile forces. Fingers form and grow in the ice concentration field, destroying the uniqueness and symmetry of the solution. The VP equations with an elliptical yield curve are stable, however, in the second sense, because the rheology always dissipates energy [Dukowicz, 1997]. The energy becomes unbounded in sea ice models as a result of the numerical discretization, not the equations themselves.

Modifications in the dynamics, including changes in the yield curve and replacement of the EVP solver with a VP solver, give little improvement. Changes in the ridging scheme, however, significantly enhance stability. The single most effective change is to replace the standard participation function P0, which gives zero strength when the open water fraction A_0 exceeds $G^* = 0.15$, with a function that varies smoothly for small changes in A_0 . Participation function P1, which decreases exponentially with $G(h)$, increases the maximum stable time step from less than 30 minutes to two hours or more in 1D and 2D test problems. For typical ITDs, P1 gives ice strengths similar to those given by P0. Thus P0 and P1 yield similar results except when P0 is unstable. We tested another function, P2, for which participation varies inversely with h^2 . P2 does not improve stability as much as P1, because it gives strengths that are very sensitive to the open water fraction for compact ice, and also because it tends to increase the participation of ice thickness than ~ 1 m.

Changing the redistribution function can also improve model stability, though less dramatically. Two alternative functions were tested. For R1, H^* is reduced from 100 m to 25 m, and for R2, the uniform ridge ITD is replaced by an ITD that falls off exponentially with thickness. R2 yields stronger ice than does a uniform ITD with the same mean thickness. When R1 or R2 is

combined with P1, the maximum stable time step for the least stable simulations increases by about 25%. Function R2 gives ridge ITDs in excellent agreement with observations, whereas the standard scheme predicts too much ice thicker than 10 m.

The *H79* strength parameterization, in which P increases linearly with the mean ice thickness, enhances stability compared to *R75*, which assumes that ice strength is proportional to ridge potential energy. However, the *H79* parameterization is less physically realistic than *R75*, and it yields relatively small maximum stress gradients that allow excessive convergence.

The highest resolution in current global and pan-Arctic sea ice models is about 10 km. With the ridging changes described here, these models can run stably with a time step of up to ~ 2 hours. Stability will also improve at finer resolutions. However, the validity of the VP rheology on scales approaching the size of individual ice floes has been questioned [Wilchinsky and Feltham, 2004a]. When sea ice models are coupled to ocean models, other stability issues may arise; in particular, there can be unstable feedbacks involving the ice-ocean stress if the coupling time scale is too long. We plan to address that issue in future work.

The numerical instability described in this paper may have escaped notice in other high-resolution simulations because it does not always crash the model. The strength and deformation fields can simply oscillate for a few days or weeks at a time, resulting in copious ridging and thick ice near topography. At the end of a run it may be impossible to say how much the ice thickness is biased by numerical noise. For this reason it is advisable to include runtime diagnostics for instability. Ice speeds greater than 1 m/s and strengths larger than 1000 kN/m, among other symptoms, usually signal a numerical problem.

Numerical robustness is a necessary but not sufficient condition for a good ridging scheme. The empirical accuracy of the standard scheme remains a source of concern. Among the unresolved issues are the following:

- What is the actual form of the participation function? Does the exponential form (57) fit real data?
- What is the shape of the redistribution function? Is it exponential over its entire range, as in (61), or only over the thick part of the ridge ITD?

- How accurate is the assumption that ice strength is proportional to ridge potential energy? To what extent does the strength depend on sliding friction?
- What are best values of the various ridging parameters? The most important are the participation parameter G^* (or a^*), the redistribution parameter H^* (or μ), the shearing/sliding parameter C_s , and the strength parameter C_f . *Kim et al.* [2006] showed that modeled sea ice thickness can be sensitive to the values of G^* , H^* , and C_f (though less so to C_s).
- What are the relative roles of mechanics (e.g., ice consolidation) and thermodynamics (e.g. preferential melting of thick ice) in converting first-year ridges to multiyear ridges? How should these processes be modeled?

Large-scale sea ice observations may not be of much help in validating ridging schemes, since other uncertainties can swamp the effects of ridging changes. However, detailed observations at smaller scales (< 100 km) could answer some of the questions above. From SAR satellite images it is possible to derive strain rates and ice thickness, which could be used to estimate ridging participation in various thickness classes. Satellite observations supplemented by surface ITD and stress measurements would aid in the validation of redistribution and strength parameterizations. Some of the necessary data may already exist but require further analysis. Numerical simulations with particle models also will continue to be useful validation tools. Such validation efforts would increase confidence that sea ice ridging schemes successfully approximate the real ice pack.

Acknowledgments

WHL and ECH were supported by the Climate Change Prediction Program (CCPP) and the Scientific Discovery through Advanced Computing (SciDAC) program of the U.S. Department of Energy's Office of Science. WM and JJ received primary support from the Shelf-Basin Interaction (SBI) program of the U.S. National Science Foundation. Additional support to WM was provided through the U.S. Department of Energy. NPS computer resources were provided by the Arctic Region Supercomputing Center (ARSC) through the U.S. Department of Defense High Performance Computer Modernization Program (HPCMP). We are grateful to John Dukowicz and Todd Ringler for many helpful discussions. We thank Julie McClean, Alison McLaren, and Pam Posey for drawing our attention to numerical instability in other sea ice simulations. We also thank Jinlun Zhang for providing his ADI code.

References

- Amundrud, T. L., H. Melling, and R. G. Ingram (2004), Geometrical constraints on the evolution of ridged sea ice, *J. Geophys. Res.*, *109*, C06005, doi:10.1029/2003JC002251.
- Babko, O., D. A. Rothrock, and G. A. Maykut (2002), Role of rafting in the mechanical redistribution of sea ice thickness, *J. Geophys. Res.*, *107* (C8), 3113, doi:10.1029/1999JC000190.
- Bitz, C. M., and W. H. Lipscomb (1999), An energy-conserving thermodynamic sea ice model for climate study, *J. Geophys. Res.*, *104*, 15,669-15,677.
- Dukowicz, J. K. (1997), Comments on “Stability of the viscous-plastic sea ice rheology,” *J. Phys. Oceanogr.*, *27*, 480-481.
- Flato, G. M., and W. D. Hibler III (1995), Ridging and strength in modeling the thickness distribution of Arctic sea ice, *J. Geophys. Res.*, *100*, 18,611-18,626.
- Gibson, J. K., P. Kallberg, S. Uppala, A. Noumura, A. Hernandez, and E. Serrano (1997): ERA Description, ECMWF Re-Analysis Project Report Series No. 1, ECMWF, Reading, UK, 77 pp.
- Gray, J. M. N. T., and P. D. Killworth (1995), Stability of the viscous-plastic sea ice rheology, *J. Phys. Oceanogr.*, *25*, 971-978.
- Gray, J. M. N. T. (1999), Loss of hyperbolicity and ill-posedness of the viscous-plastic sea ice rheology in uniaxial divergent flow, *J. Phys. Oceanogr.*, *29*, 2920-2929.
- Hibler, W. D., III (1977), A viscous sea ice law as a stochastic average of plasticity, *J. Geophys. Res.*, *82*, 3932-3938.
- Hibler, W.D., III (1979), A dynamic thermodynamic sea ice model, *J. Phys. Oceanogr.*, *9*, 815-846.
- Hibler, W. D., III (1980), Modeling a variable thickness sea ice cover, *Mon. Wea. Rev.*, *108*, 1943-1973.
- Hibler, W. D., III, and J. E. Walsh (1982), On modeling seasonal and interannual fluctuations of Arctic sea ice, *J. Phys. Oceanogr.*, *12*, 1514-1523.

- Holland, M. M., C. M. Bitz, E. C. Hunke, W. H. Lipscomb, and J. L. Schramm (2006), Influence of the sea ice thickness distribution on polar climate in CCSM3, *J. Climate*, *19*, 2398-2414.
- Hopkins, M. A. (1994), On the ridging of intact lead ice, *J. Geophys. Res.*, *99*, 16,351-16,360.
- Hopkins, M. A. (1998), Four stages of pressure ridging, *J. Geophys. Res.*, *103*, 21,883-21,891.
- Hunke, E. C. (2001), Viscous-plastic sea ice dynamics with the EVP model: Linearization issues, *J. Comput. Phys.*, *170*, 18-38.
- Hunke, E. C., and J. K. Dukowicz (1997), An elastic-viscous-plastic model of sea ice dynamics, *J. Phys. Oceanogr.*, *27*, 1849-1867.
- Hunke, E. C., and J. K. Dukowicz (2002), The elastic-viscous-plastic sea ice dynamics model in general orthogonal curvilinear coordinates on a sphere—Incorporation of metric terms, *Mon. Wea. Rev.*, *130*, 1848-1865.
- Hunke, E. C., and W. H. Lipscomb (2004), CICE: The Los Alamos Sea Ice Model, documentation and software, Version 3.1, LA-CC-98-16, Los Alamos Natl. Lab., Los Alamos, NM, 56 pp.
- Hutchings, J. K., H. Jasak, and S. W. Laxon (2004), A strength implicit correction scheme for the viscous-plastic sea ice model, *Ocean Model.*, *7*, 111-133.
- Kim, J., E. C. Hunke, and W. H. Lipscomb (2006), Sensitivity analysis and parameter tuning scheme for global sea-ice modeling, submitted to *Ocean Model.*
- Kållberg, P., A. Simmons, S. Uppala and M. Fuentes (2004), The ERA-40 Archive, ERA-40 Project Report Series No. 17, ECMWF, Reading, UK, 35 pp.
- Kwok, R., and G. F. Cunningham (2002), Seasonal ice area and volume production of the Arctic Ocean: November 1996 through April 1997, *J. Geophys. Res.*, *107* (C10), 8038, doi:10.1029/2000JC000469.
- Lepparanta, M., M. Lensu, P. Kosloff, and B. Veitch (1995), The life story of a first-year sea ice ridge, *Cold Reg. Sci. Technol.*, *20*, 295-311.
- Lipscomb, W. H. (2001), Remapping the thickness distribution in sea ice models, *J. Geophys. Res.*, *106*, 13,989-14,000.

- Lipscomb, W. H., and E. C. Hunke (2004), Modeling sea ice transport using incremental remapping, *Mon. Wea. Rev.*, 132, 1341-1354.
- Maslowski, W., and W. H. Lipscomb (2003), High resolution simulations of Arctic sea ice, 1979-1993, *Polar Research*, 22(1), 67-74.
- Maslowski, W., D. Marble, W. Walczowski, U. Schauer, J. L. Clement, and A. J. Semtner (2004), On climatological mass, heat, and salt transports through the Barents Sea and Fram Strait from a pan-Arctic coupled ice-ocean model simulation, *J. Geophys. Res.*, 109, C03032, doi:10.1029/2001JC001039.
- McLaren, A., H. Banks, C. Durman, J. Gregory, T. Johns, A. Keen, J. Ridley, M. Roberts, W. Lipscomb, W. Connolley, and S. Laxon (2006), Evaluation of the sea ice simulation in a new atmosphere-ocean coupled climate model (HadGEM1), submitted to *J. Geophys. Res.*
- National Snow and Ice Data Center (2005), Submarine upward looking sonar ice draft profile data and statistics, National Snow and Ice Data Center/World Data Center for Glaciology, Boulder, CO. Digital media.
- Parmerter, R. R., and M. D. Coon (1972), Model of pressure ridge formation in sea ice, *J. Geophys. Res.*, 77, 6565-6575.
- Pritchard, R. S. (2005), Stability of sea ice dynamics models: Viscous-plastic rheology, replacement closure, and tensile cutoff, *J. Geophys. Res.*, 110, C12010, doi:10.1029/2003JC001875.
- Richter-Menge, J., and B. C. Elder (1998), Characteristics of pack ice in the Alaskan Beaufort Sea, *J. Geophys. Res.*, 103, 21,817-21,829.
- Richter-Menge, J., S. L. McNutt, J. E. Overland, and R. Kwok (2002), Relating Arctic pack ice stress and deformation under winter conditions, *J. Geophys. Res.*, 107 (C10), 8040, doi:10.1029/2000JC000477.
- Rothrock, D. A. (1975), The energetics of the plastic deformation of pack ice by ridging, *J. Geophys. Res.*, 80, 4514-4519.
- Smith, R. D., M. E. Maltrud, F. O. Bryan, and M. W. Hecht (2000), Numerical simulation of the North Atlantic Ocean at $\frac{1}{10}^\circ$, *J. Phys. Oceanogr.*, 30, 1532-1561.

- Stern, H. L., D. A. Rothrock, and R. Kwok (1995), Open water production in Arctic sea ice: Satellite measurements and model parameterizations, *J. Geophys. Res.*, *100*, 20,601-20,612.
- Thorndike, A. S., D. A. Rothrock, G. A. Maykut, and R. Colony (1975), The thickness distribution of sea ice, *J. Geophys. Res.*, *80*, 4501-4513.
- Tucker, W. B. III, D. S. Sodhi, and J. W. Govoni (1984), Structure of first-year pressure ridge sails in the Prudhoe Bay region, in *The Alaskan Beaufort Sea: Ecosystems and Environments*, edited by P. W. Barnes, D. M. Schell, and E. Reimnitz, Academic Press, London, 115-135.
- Ukita, J., and R. E. Moritz (2000), Geometry and the deformation of pack ice: II. Simulation with a random isotropic model and implication in sea-ice rheology, *Ann. Glaciol.*, *31*, 323-326.
- Vinje, T., N. Nordlund, and Å. Kvambekk (1998), Monitoring ice thickness in Fram Strait, *J. Geophys. Res.*, *103*, 10,437-10,449, 1998.
- Wilchinsky, A. V., and D. L. Feltham (2004a), A continuum anisotropic model of sea-ice dynamics, *Proc. R. Soc. Lond. A*, *460*, 2105-2140.
- Wilchinsky, A. V., and D. L. Feltham (2004b), Dependence of sea ice yield-curve shape on ice thickness, *J. Phys. Oceanogr.*, *34*, 2852-2856.
- Zhang, J., and W. D. Hibler III (1997), On an efficient numerical method of modeling sea ice dynamics, *J. Geophys. Res.*, *102*, 8691-8702.
- Zhang, J., and D. A. Rothrock (2000), Modeling sea ice with an efficient plastic solution, *J. Geophys. Res.*, *105*, 3325-3338.
- Zhang, J., and D. A. Rothrock (2005), Effect of sea ice rheology in numerical investigations of climate, *J. Geophys. Res.*, *110*, C08014, doi:10.1029/2004JC002599.

Figure Captions

Figure 1. Unstable ice fields in the Canadian Archipelago on 2 July 1979 of a standalone Arctic sea ice run with standard ridging parameters. (a) Fractional ice concentration. (b) Mean ice thickness (m). (c) Ice strength (kN/m). (d) Divergence (%/day). The scales of (a), (c), and (d) are stretched to show extreme values.

Figure 2. Maximum values of various fields during year 1 of a standalone Arctic sea ice run with standard ridging parameters (solid lines) and with the standard participation function $b(h)$ replaced by an exponential function (dashed lines). The entire grid is sampled once per day; the maximum value on the grid is plotted. (a) Mean ice thickness (m). (b) Ice speed (m/s). (c) Internal ice stress divergence (Pa). (d) Ridging rate, defined as the percentage area of ice ridged per day. The standard $b(h)$ gives unstable flow from late June until early fall. During stable periods, the two forms of $b(h)$ give similar results.

Figure 3. Model fields after 1, 5, and 30 days of the 1D test case with multiyear ice (ITD1) flowing toward a fixed eastern boundary, with $\Delta t = 5$ minutes. (a) Ice speed (m/s). (b) Ice strength (kN/m).

Figure 4. Eastward ice velocity (m/s) and strength (kN/m) after days 1 and 5 of a 1D test case simulation, initialized with ITD3 (5-m ice with 20% open water) and run with three different time steps. (a) Velocity, day 1. (b) Velocity, day 5. (c) Strength, day 1. (d) Strength, day 5. With $\Delta t = 5$ minutes the run is stable throughout; with $\Delta t = 30$ minutes there are oscillations after day 1, which have mostly damped out by day 5; and with $\Delta t = 60$ minutes the oscillations persist through day 5.

Figure 5. Mean kinetic energy (J/m^2) per grid cell as a function of time for the 1D test case, initialized with each of three ice thickness distributions and run with various time steps. (a) ITD1,

typical multiyear ice. (b) ITD2, uniform 5-m ice. (c) ITD3, 5-m ice with 20% open water. Unstable runs can terminate before day 30 with advective CFL violations. The energy scale for (a) is different from that for (b) and (c).

Figure 6. Ice fields from two simulations on a 10-km test grid with an L-shaped island. One simulation is run with the standard participation function $b(h)$ and the other with an exponential $b(h)$. The runs are initialized with ITD3 (5-m ice with 20% open water). The model is run for 24 hours with a time step of 30 minutes, forced by a uniform wind $u = v = 10$ m/s. (a) Fractional ice concentration, standard $b(h)$. (b) Divergence (%/day), standard $b(h)$. (c) Fractional ice concentration, exponential $b(h)$. (d) Divergence (%/day), exponential $b(h)$. The color scales on the top and bottom plots are identical.

Figure 7. Ice fields in the Canadian Archipelago on 2 July 1979 of a standalone Arctic sea ice run. The model parameters and forcing are the same as in Figure 1, except that the standard participation function P0 is replaced by the exponential function P1. (a) Fractional ice concentration. (b) Mean ice thickness (m). (c) Ice strength (kN/m). (d) Divergence (%/day). The color scales are the same as in Figure 1; note the absence of extreme values.

Figure 8. The e -folding scale for the exponential tail of the ITD is plotted against mean ice draft. Each data point represents one 50-km submarine track in the Arctic Ocean. A total of 1661 tracks are included from 22 cruises between 1976 and 1999 [NSIDC, 2005]. Tracks with fewer than 1000 drafts greater than 5 m are excluded. The e -folding scale is computed by least-squares regression of $\log[g(D)]$ against the draft D for $D > 5$ m.

Table 1. Maximum stable time step in minutes for the 1D test problem

Case	ITD1	ITD2	ITD3
Standard (P0, R0)	175	90	25
P1, R0	225	115	155
P2, R0	80	40	50
P0, R1	200	135	50
P0, R2	185	120	25
P1, R1	220	165	145
P1, R2	215	150	165

The table shows the maximum stable time step in minutes for various combinations of the participation function, redistribution function, and initial ITD. For each case CICE is run on a 10-km grid with open periodic north-south boundaries and closed east-west boundaries. The ice is forced toward the eastern boundary by a westerly wind for up to 30 days. A run is considered unstable if an advective CFL violation occurs or if the maximum ice velocity exceeds 0.5 m/s. Initial ITDs are as follows: ITD1 = typical multiyear ice, ITD2 = uniform 5-m ice, ITD3 = 5-m ice with 20% open water. The participation functions (P0, P1, and P2) and redistribution functions (R0, R1, and R2) are defined in the text.

Table 2. Maximum stable time step in minutes for the 2D test problem

Case	ITD1	ITD2	ITD3
Standard (P0, R0)	160	55	20
P1, R0	350	265	295
P2, R0	65	25	75
P0, R1	180	85	30
P0, R2	185	70	25
P1, R1	375	270	295
P1, R2	350	265	295

The table shows the maximum stable time step in minutes for various combinations of the participation function, redistribution function, and initial ITD. For each case CICE is run on a 10-km grid with open periodic boundaries. The ice is forced past an L-shaped island by a southwesterly wind for up to 30 days. A run is considered unstable if an advective CFL violation occurs or if the maximum ice velocity exceeds 0.5 m/s. Participation and redistribution functions and initial ITDs are as defined for Table 1. Details are given in the text.

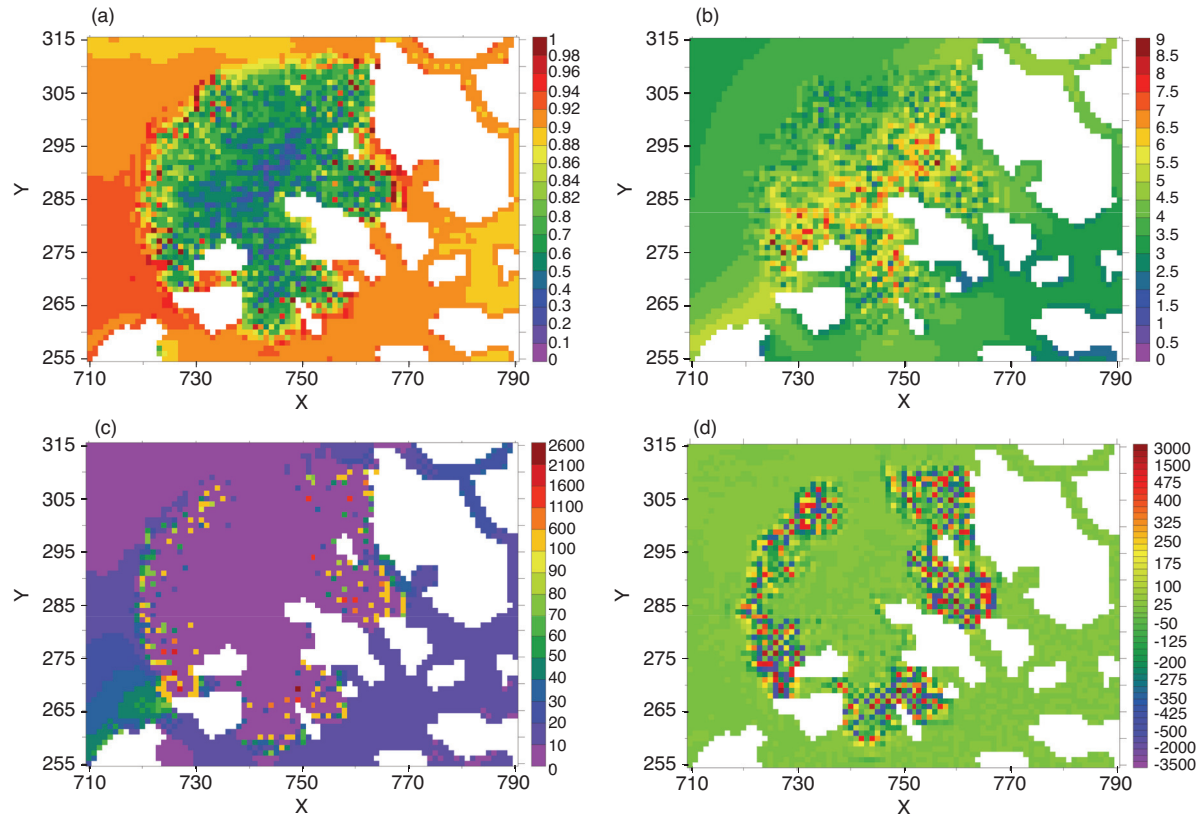


Figure 1. Unstable ice fields in the Canadian Archipelago on 2 July 1979 of a standalone Arctic sea ice run with standard ridging parameters. (a) Fractional ice concentration. (b) Mean ice thickness (m). (c) Ice strength (kN/m). (d) Divergence (%/day). The scales of (a), (c), and (d) are stretched to show extreme values.

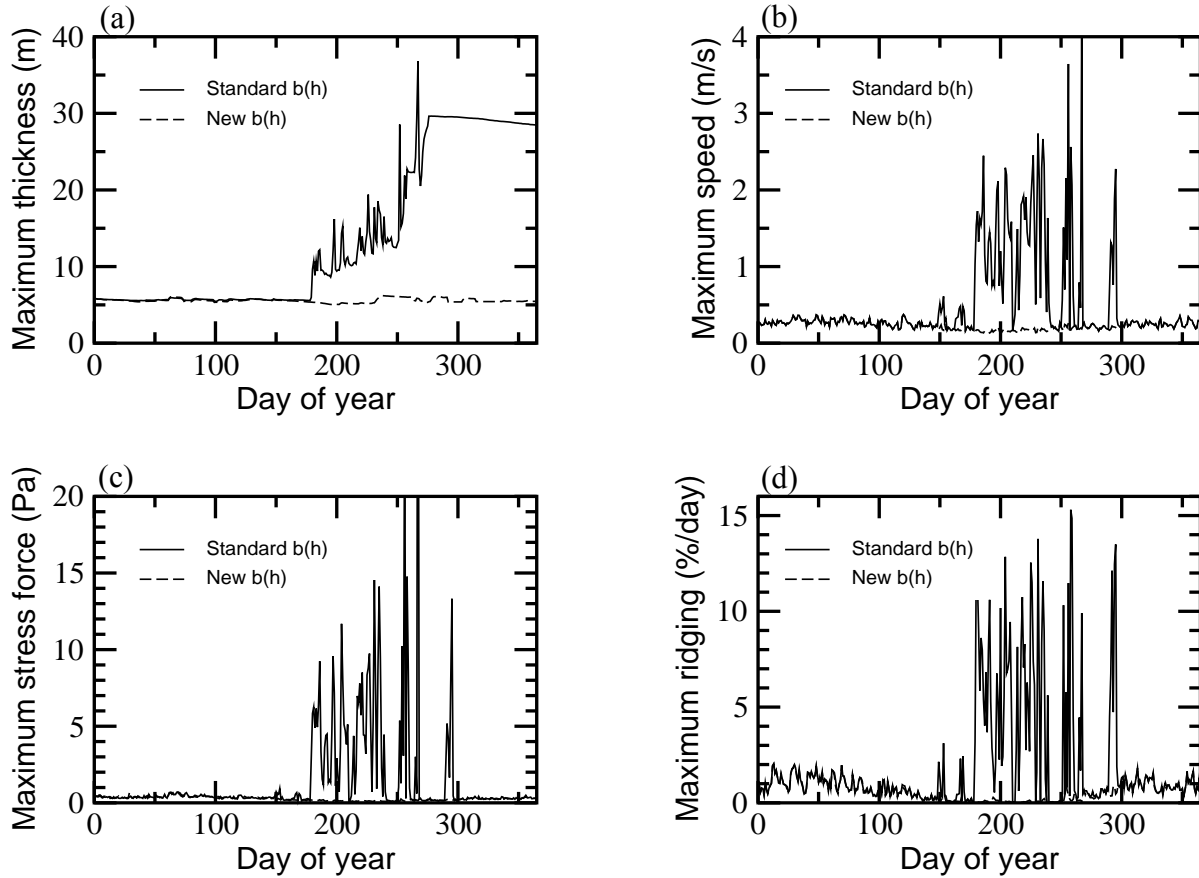


Figure 2. Maximum values of various fields during year 1 of a standalone Arctic sea ice run with standard ridging parameters (solid lines) and with the standard participation function $b(h)$ replaced by an exponential function (dashed lines). The entire grid is sampled once per day; the maximum value on the grid is plotted. (a) Mean ice thickness (m). (b) Ice speed (m/s). (c) Internal ice stress divergence (Pa). (d) Ridging rate, defined as the percentage area of ice ridged per day. The standard $b(h)$ gives unstable flow from late June until early fall. During stable periods, the two forms of $b(h)$ give similar results.

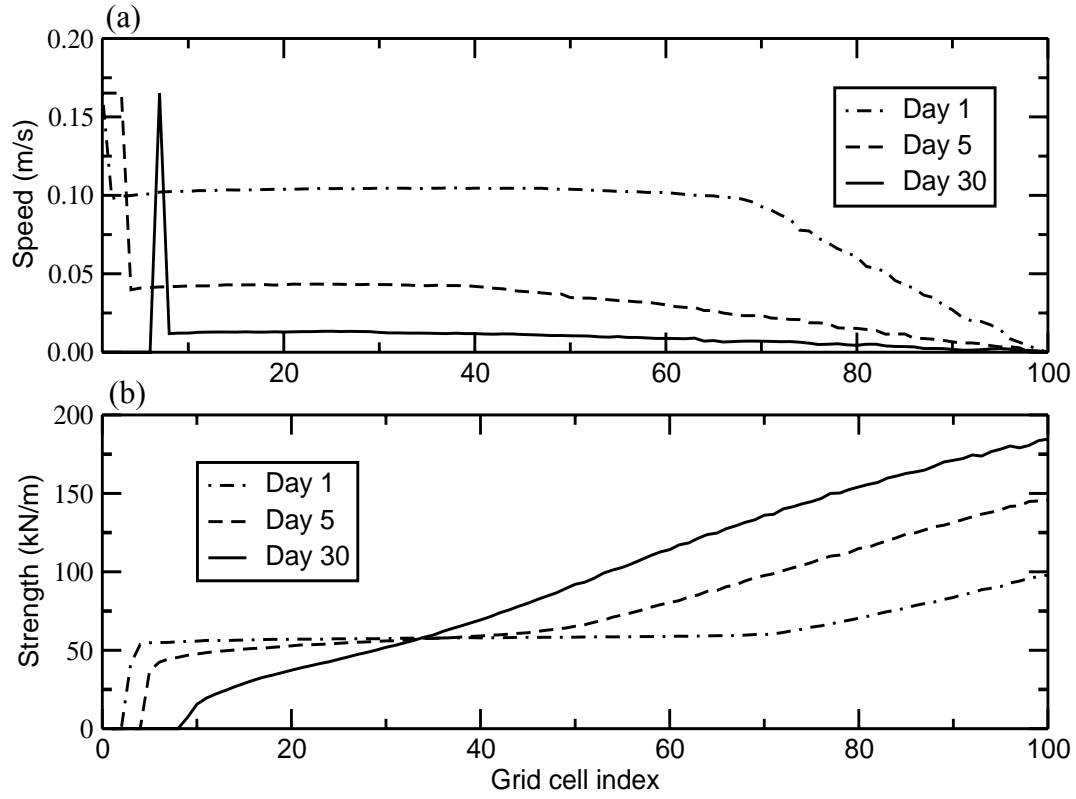


Figure 3. Model fields after 1, 5, and 30 days of the 1D test case with multiyear ice (ITD1) flowing toward a fixed eastern boundary, with $\Delta t = 5$ minutes. (a) Ice speed (m/s). (b) Ice strength (kN/m).

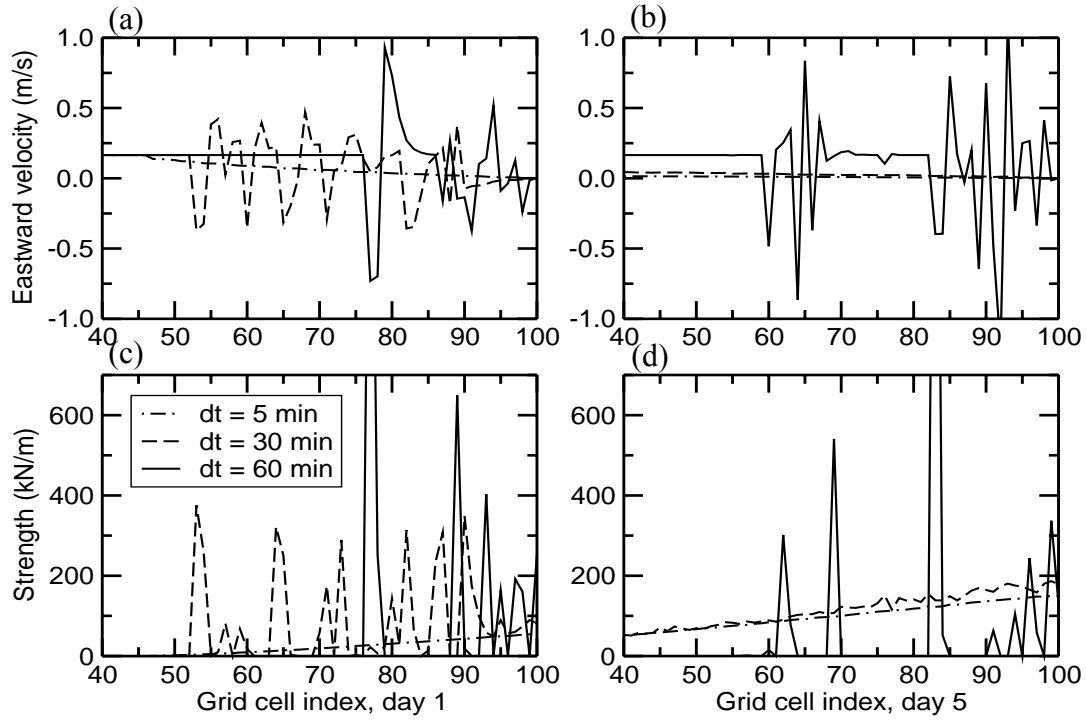


Figure 4. Eastward ice velocity (m/s) and strength (kN/m) after days 1 and 5 of a 1D test case simulation, initialized with ITD3 (5-m ice with 20% open water) and run with three different time steps. (a) Velocity, day 1. (b) Velocity, day 5. (c) Strength, day 1. (d) Strength, day 5. With $\Delta t = 5$ minutes the run is stable throughout; with $\Delta t = 30$ minutes there are oscillations after day 1, which have mostly damped out by day 5; and with $\Delta t = 60$ minutes the oscillations persist through day 5.

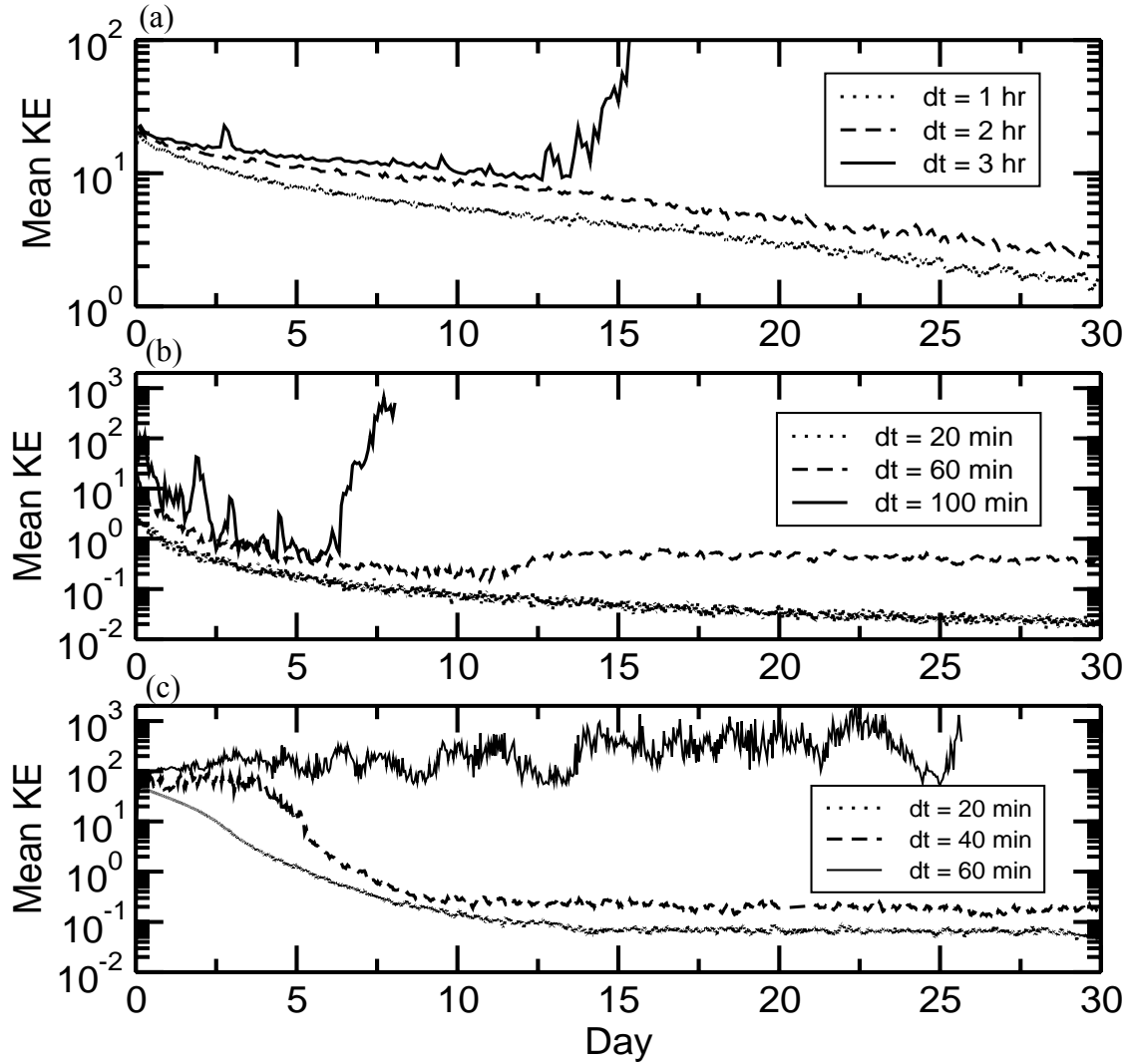


Figure 5. Mean kinetic energy (J/m^2) per grid cell as a function of time for the 1D test case, initialized with each of three ice thickness distributions and run with various time steps. (a) ITD1, typical multiyear ice. (b) ITD2, uniform 5-m ice. (c) ITD3, 5-m ice with 20% open water. Unstable runs can terminate before day 30 with advective CFL violations. The energy scale for (a) is different from that for (b) and (c).

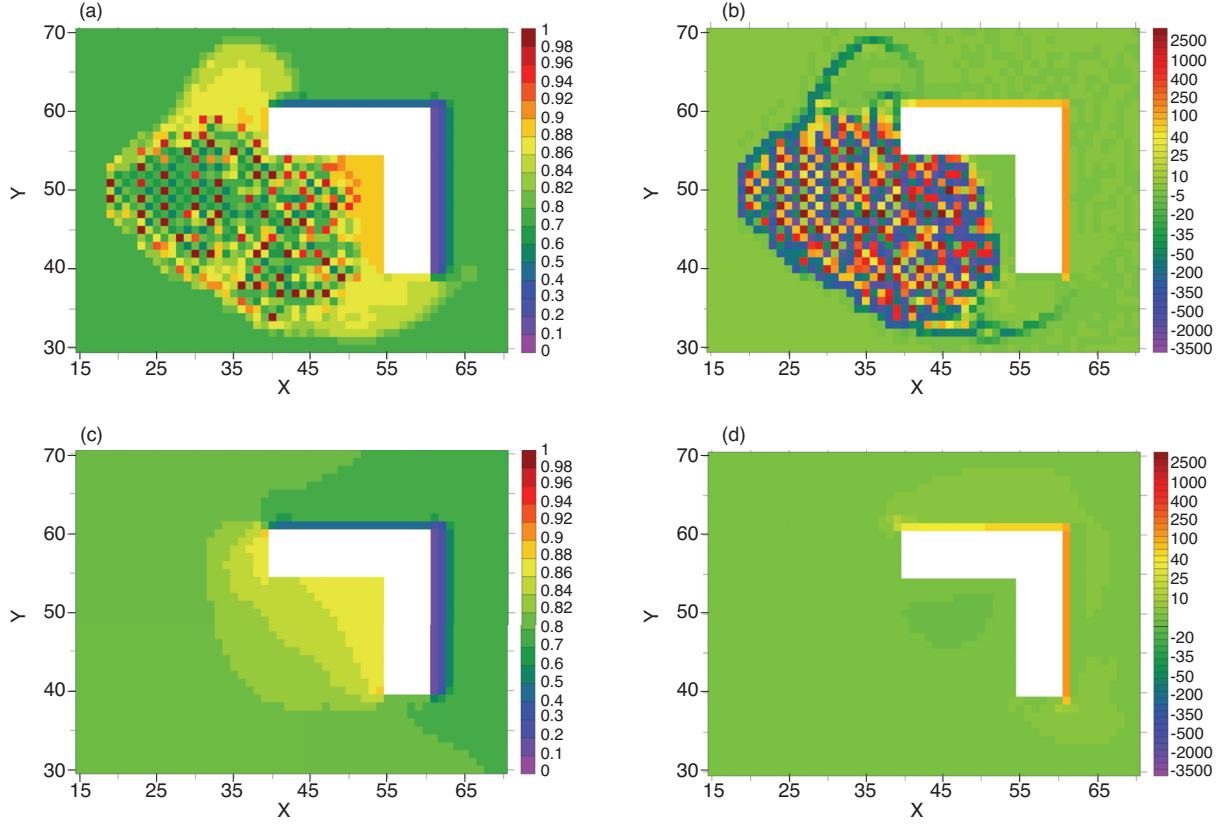


Figure 6. Ice fields from two simulations on a 10-km test grid with an L-shaped island. One simulation is run with the standard participation function P0 and the other with the exponential function P1. The runs are initialized with ITD3 (5-m ice with 20% open water). The model is run for 24 hours with a time step of 30 minutes, forced by a uniform wind $u = v = 10$ m/s. (a) Fractional ice concentration, P0. (b) Divergence (%/day), P0. (c) Fractional ice concentration, P1. (d) Divergence (%/day), P1. The color scales on the top and bottom plots are identical.

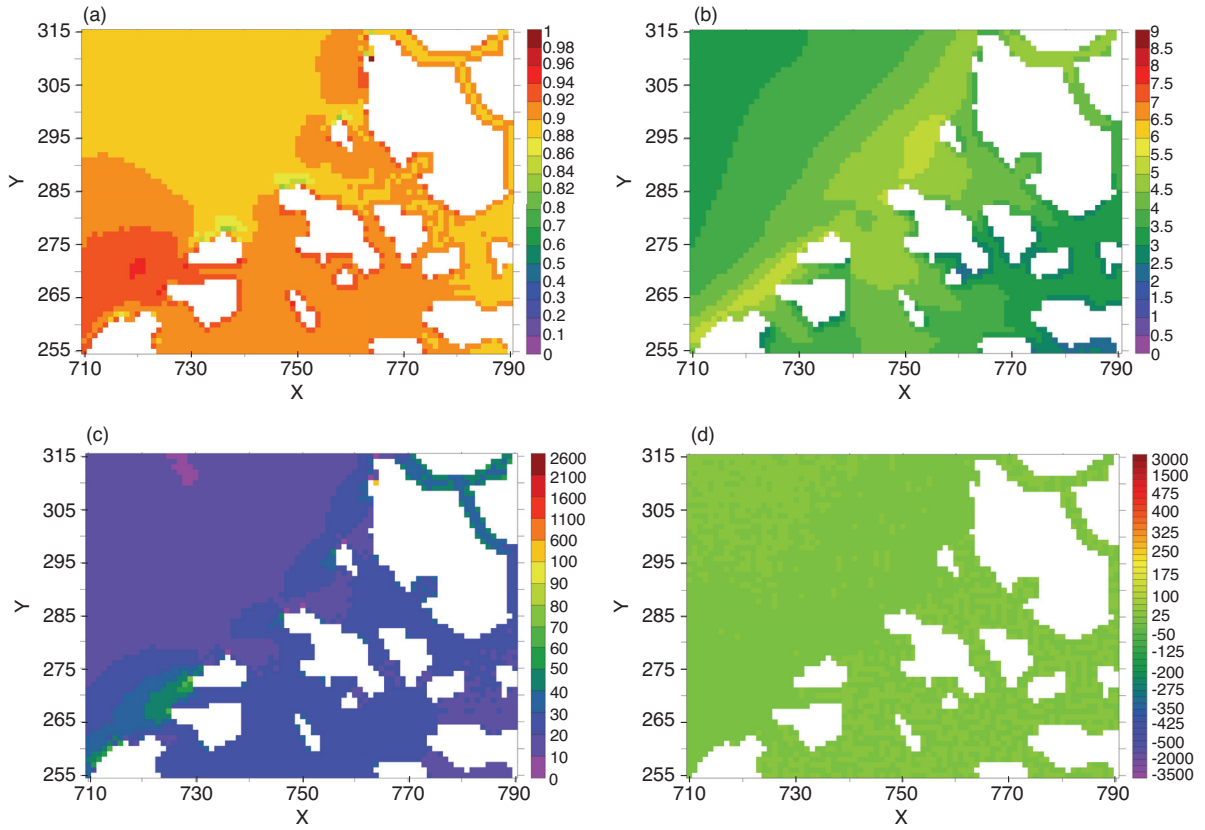


Figure 7. Ice fields in the Canadian Archipelago on 2 July 1979 of a standalone Arctic sea ice run. The model parameters and forcing are the same as in Figure 1, except that the standard participation function P0 is replaced by the exponential function P1. (a) Fractional ice concentration. (b) Mean ice thickness (m). (c) Ice strength (kN/m). (d) Divergence (%/day). The color scales are the same as in Figure 1; note the absence of extreme values.

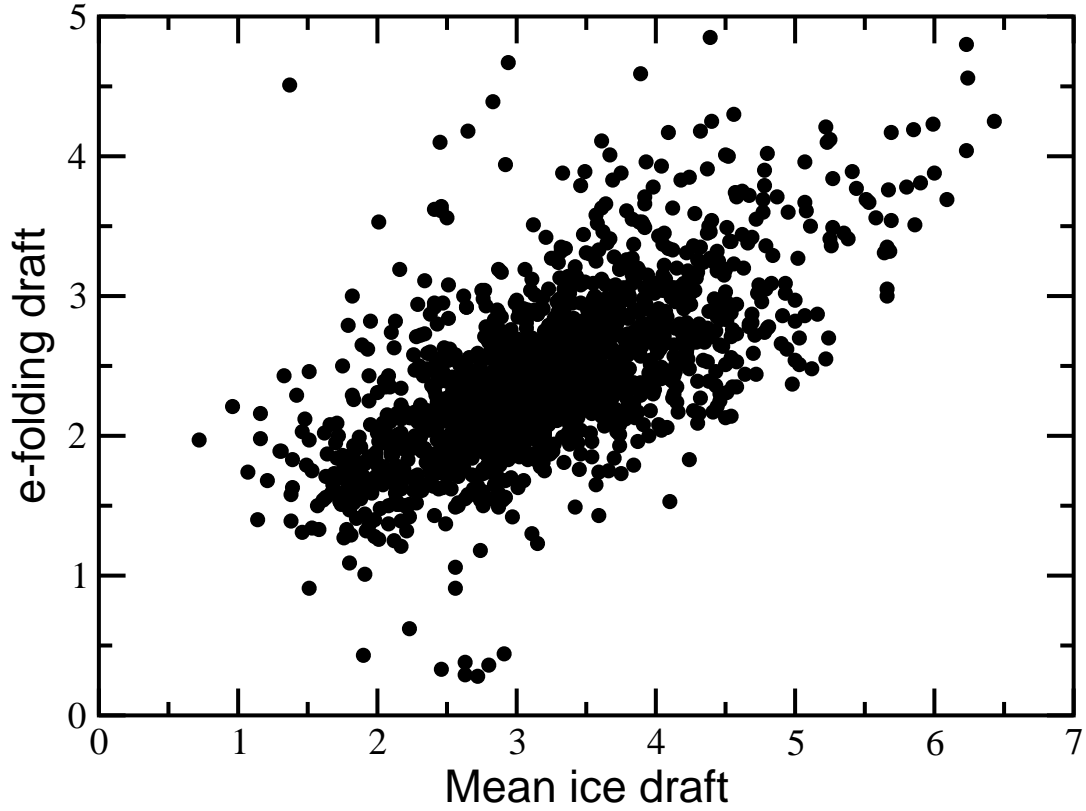


Figure 8. The e -folding scale for the exponential tail of the ITD is plotted against mean ice draft. Each data point represents one 50-km submarine track in the Arctic Ocean. A total of 1661 tracks are included from 22 cruises between 1976 and 1999 [NSIDC, 2005]. Tracks with fewer than 1000 drafts greater than 5 m are excluded. The e -folding scale is computed by least-squares regression of $\log[g(D)]$ against the draft D for $D > 5$ m.